2018

The Fate and One-Dimensional Transport of Creighton Colloidal Silver Nanoparticles Through Saturated Porous Media

Jessica M. Dagher
Wright State University

THE FATE AND ONE DIMENSIONAL TRANSPORT OF CREIGHTON COLLOIDAL SILVER NANOPARTICLES THROUGH SATURATED POROUS MEDIA

A thesis submitted in partial fulfillment of the

requirements for the degree of

Master of Science

By

JESSICA M. DAGHER

B.S., Wright State University, 2010

2018
Wright State University

WRIGHT STATE UNIVERSITY
GRADUATE SCHOOL

December 2013

I HEREBY RECOMMEND THAT THE THESIS PREPARED UNDER MY SUPERVISION BY Jessica M. Dagher ENTITLED the fate and one-dimensional transport of Creighton colloidal silver nanoparticles through saturated porous media BE ACCEPTED IN PARTIAL FULFILMENT OF THE REQUIREMENTS FOR THE DEGREE OF Master of Science.

_____
Ioana E. Sizemore, Ph.D.
Thesis Director

_____
David A. Grossie, Ph.D.
Chair, Department of Chemistry

Committee on
Final Examination

_____
Ioana E. Sizemore, Ph.D.

_____
Rachel Aga, Ph.D.

_____
David A. Dolson, Ph.D.

_____
Mark N. Goltz, Ph.D.

_____
Sushil R. Kanel, Ph.D., Honorary Member

_____
Barry Milligan, Ph.D.
Interim Dean, Graduate School

ABSTRACT

Dagher, Jessica M. M.S., Department of Chemistry, Wright State University. 2018. The fate and one-dimensional transport of Creighton colloidal silver nanoparticles through saturated porous media.

With the ubiquitous burst of nanotechnology, silver nanoparticles (AgNPs) have become indispensable in numerous industrial, medicinal, and research applications. Consequently, AgNPs have been alarmingly disposed into subsurface water increasing the risk of human and environmental exposure. While mechanisms of AgNP cytotoxicity have been reported, research studies on AgNP transport in subsurface water are needed, according to U.S. Environmental Protection Agency (EPA). The main goal of this study was to investigate the environmental fate and transport of widely-used Creighton colloidal AgNPs in a laboratory transport system simulating a porous, saturated groundwater aquifer. To achieve this, a large volume of AgNPs was synthesized, characterized using a suite of well-established analytical and microscopy techniques, and manipulated by tangential flow filtration. AgNPs and a conservative tracer, Cl^- as a potassium chloride solution, were pulse-injected upward through a one-dimensional laboratory column (5 cm in depth, 2.5 cm diameter) at fixed pH, flow rate, and ionic strength, and pore volume. Breakthrough curves for AgNP transport were constructed using UV-Vis absorption, flame atomic absorption spectroscopy (FAAS) and inductively coupled plasma optical emission spectroscopy (ICP-OES). Smaller AgNPs (1−20 nm in diameter) were found to elute faster than larger AgNPs (1−100 nm in diameter). Flow rate and AgNP size were found to influence the sorption of AgNPs onto the media, as evidenced by the size and shape of the

non-equilibrium breakthrough curves. Facilitated transport was attributed to moderate electrostatic repulsions between the negatively charged AgNPs and the polar glass beads. The transport of the AgNPs through the one dimensional laboratory system and the accurate ICP-OES-based quantification of nanosilver concentration in colloidal samples were translated into two novel laboratory experiment modules, which were successfully implemented into the *Experimental Nanomaterials and Nanoscience* course and the *Instrumental Analysis* laboratory course at WSU respectively.

TABLE OF CONTENTS

LIST OF FIGURES

LIST OF TABLES

ACKNOWLEDGEMENTS

First and foremost, I offer my gratitude to my research advisor, Dr. Ioana E. Pavel Sizemore, for her work and thorough commitment in presenting me with the opportunity of conducting research.

I express my gratitude to the Chemistry Department of Wright State University, and the Air Force Institute of Technology at the Wright Patterson Air Force Base, in Dayton, Ohio, for technical and financial support, which has rendered my completion of the Master degree requirements possible. I extend my appreciation to Dr. Sushil R. Kanel for his great mentorship and his experimental guidance with the characterization measurements of my silver nanomaterials (TEM, ion chromatography, and Zeta potential), and Dr. Mark N. Goltz for his supervision of the theoretical and the computational aspects of the project. Finally, I thank my research group members for their assistance, Dr. Marjorie Markopoulos and Dr. Daniel Felker for their laboratory safety training and guidelines. Last and not least, I thank Dr. David Dolson for his relentless academic guidance during my undergraduate and graduate studies. I want to thank Dr. Arathi Paluri and Dr. Marjorie Markopoulos for supporting me and sharing their expertise on numerous laboratory concepts.

I am excited to see this project to completion and look forward for the future endeavors that will take relevant environmental research to the next level

1. INTRODUCTION

1.1. APPLICATIONS OF SILVER NANOMATERIALS (AGNMS)

Nanoscience and nanotechnology are highly interdisciplinary domains, which have recently surged in popularity and importance [1, 2] and thus, experienced an exponential increase in funding. For example, the National Nanotechnology Initiative (NNI), which was implemented by President Clinton in 2000 [2] and authorized in 2003 [2b], increased the research and development (R&D) funding from $270 million in 2000 [2] to $1.847 billion in 2011 [3]. In 2018, about 1.2 billion is projected as Federal Budget dedicated for the National Nanotechnology Initiative [2b]. Accordingly, the number of participating agencies also increased from seven in 2000 to 26 in 2012. A few examples include the National Science Foundation (NSF), the National Institutes of Health (NIH), the Department of Energy (DOE), the National Aeronautics and Space Administration (NASA), the Environmental Protection Agency (EPA), and so on [3]. In the areas of research and development, a revenue of $3.7 trillion is projected for 2018 in nanotechnology enabled products on the U.S. marketplace [2b].

A nanomaterial (NM) consists of ultrafine particulate matter that satisfies at least one of the following criteria: a) “one or more external dimensions in the size range 1 nm − 100 nm for more than 1% of their number size distribution”, b) “at least one internal or surface structure dimension in the size range 1 nm − 100 nm”,

and c) "a specific surface area by volume greater than 60 m^2 cm^{-3}, excluding materials consisting of particles with a size lower than 1 nm" [4]. The size range and distribution are reinforced for uniform interpretation. As of 2010, more than 1000 consumer products containing NMs of 1−100 nm in size were on the global market [1b]. The Project on Emerging Nanotechnologies inventory [5a] continuously updates the consumer product inventory (CPI) in the U.S. and worldwide [5b]. The updated inventory indicates a rise from 54 to 1814 nanomaterial based products, between 2005 and 2015 in 32 countries, with the health and fitness sector making 42% [5b] as well as the U.S. being the lead producer (48 % as of 2013) [5a]. Most of these consumer-based applications exploit the well-known antimicrobial properties of silver. Silver has been used for millennia as a broad-spectrum biocide [6, 7] in bulk, ionic and nanomaterial form, especially for antibiotic-resistant microbial strains [8]. Silver benefits date back to ancient civilizations, such as Greeks and Romans, who sterilized water using silver [8, 9] prior to the development of antibiotics [10]. In World War I, silver was intensively utilized to fight infections [11], but its applications declined after World War II upon the advent of antibiotics [12]. Silver's popularity resurged with the scientific advancement of nanomaterials (NMs) during the past few decades.

The nanomaterial form of silver and other noble metals gives rise to physicochemical properties [13, 14] (optical, electric, magnetic, catalytic, *etc.*) that are absent in the bulk form [15, 16]. Nowadays, AgNMs are employed as highly efficient, broad-spectrum biocides (anti- microbial [6, 8, 17, 18], viral [7], and fungal [6]). The NM based, consumer products are classified into the following categories,

as of 2014: Health and Fitness (**505** or 42%); Home and Garden (**246** or 20.5%); Automotive (**152** or 12.6%); Food and Beverage (**72** or 6%); Cross Cutting (**95** or 7.9%); Electronics and Computers (**70** or 5.8%); Appliances (**39** or 3.2%); Children Goods (**23** or 1.9%) [5b Vance et al].

Silver use in NM based products has grown exponentially since 2006. Of the claimed, nanomaterial-composition categories detailed in the updated (2015) CPI inventory [5b], AgNMs are used in 438 products or 24% (including 141 nanosilver products listed in the European inventory in 2012 [5b]) and are the most popular in advertisement, though they rank second to metals and metal oxides (37%) [5b Vance 2015].

According to the U.S. NNI fund projections report for 2018, nanotechnology plays a growing role in the high tech (HT) or knowledge intensive industries, which accounted for 15% of the global manufacturing sector in 2014 and added $511 billion to the U.S. gross domestic product (GDP) [2b]. The HT industries also created 1.8 million high-paying U.S. jobs in 2014, and while they only accounted for three percent of the U.S. GDP, they funded almost half the U.S. R&D sector [2b]. The U.S. Nanoscale Science, Engineering, and Technology (NSET) Subcommittee works with several other groups to set long term goals for the NNI and to keep U.S. as a world leader in nanotechnology [2b]. Some of the NSET Subcommittee goals projected for 2016-2018 period include water sustainability, sensor and nanoelectronics development in safety and environment, and sustainable manufacturing [2b]. For example, the U.S. Department of Agriculture (USDA) collaborated with researchers to develop a graphene-based

sensor that detects pesticides in water and soil with the purpose of alleviating their environmental impact [2b]. Furthermore, significant savings in energy have been projected since 2004 for its consumption in U.S. and other countries [1].

AgNMs have been explored for water treatment [5, 15, 19, 20]. Due to their optical capabilities, AgNMs find applications in metal-enhanced, fluorescence immunoassay- and surface-enhanced Raman-spectroscopy- based detection of pathogen (*e.g.*, viruses such as *Hepatitis B* and *human immunodeficiency virus* (HIV), bacteria (*e.g.*, *Bacillus anthracis*) and tumor markers at very low concentrations [21, 22, 23, 24] in the femtomolar level [21]. Furthermore, integration of AgNMs in efficient, noninvasive, diagnostic and therapeutic systems has shown potential to eliminate otherwise harsh, nonselective methods, such as ionizing irradiation [13, 24]. In one study, cancerous glioma cells were selectively sensitized to infrared radiation (IR) by local exposure to silver nanoparticles (AgNPs), the most heavily used form of nanosilver. Its success was attributed to the release of ionic silver (Ag^+) from AgNPs and the subsequent formation of reactive oxygen species (ROS) at cancer sites [25]. When administered in conjunction with *Albizia adianthifolia*, a plant that induces cancer cell arrest, AgNPs were proven to exhibit anticarcinogenic effects in mammalian, A459 lung carcinoma cells by inducing mitochondrial damage and an intrinsic apoptotic pathway [26]. More recently, security-, defense- [1] and solar energy- [27] -related applications of AgNMs utilize their conductive, plasmonic, and (photo)catalytic properties in nanocomposite systems (*e.g.*, nanowires that enhance thermal and electrical conductivity [28]).

1.2. ENVIRONMENTAL IMPLICATIONS OF SILVER NANOMATERIALS (AGNMS)

Several reasons necessitate assessment of the transport of AgNMs: a) their benefit to nanoscience development and the inevitable need for their disposal [1], b) their use in water remediation (*e.g.*, removal of microorganisms [19] and catalytic removal of organic compounds such as halocarbons or pesticides [20, 29]), c) the gap in knowledge of their long-term interaction with ecologic systems and the potential adverse effects on human health and environment [14, 30], d) the difficulties in the water treatment process due to the presence of silver [31], and e) the importance of clean water resources in eliminating hygienic ailments and government spending (over 1 billion individuals are affected worldwide daily because of the lack of clean water resources) [32].

1.2.1. POTENTIAL SOURCES OF EXPOSURE AND OCCUPATIONAL LIMITS OF SILVER:

Potential sources of human exposure to Ag include photographic material, dental amalgams, medical devices, antiseptic dressings, and so on. Argyria was reported as a result of gastrointestinal or parenteral intake and confirmed for a dose equal to or exceeding 5 g kg^{-1} [33]. Baseline concentrations of Ag in human tissue were determined spectrochemically to be 2.3 μg L^{-1} in blood, 2 μg day^{-1} in urine, and 0.05 μg g^{-1} in liver and kidney wet tissue [33]. While no occupational exposure limits were established for nanosilver yet [34], the U.S. EPA has recommended

further evaluation of acute and chronic limits [1, 35] in order to protect human health, aquatic and wild life. Occupational limits for other forms of Ag are given in Table 1. The primary maximum contaminant level (MCL) for Ag was withheld in 1989, while the Ag criteria were updated four times between 1981 and 1994 [35]. The 0.05 μg mL^{-1} limit of Ag set by U.S. EPA for drinking water was removed in 1989. U.S. EPA has since introduced a short term 1-10-day drinking water exposure limit for Ag at 1.142 mg L^{-1} [36a]. More recently, the World Health Organization (WHO) gave a lower maximum value of 0.1 mg L^{-1} for silver among its guidelines for drinking water contaminant levels [36b] agreeing with the most recent EPA secondary maximum contaminant level (SMCL) as **0.1 mg L^{-1}** on the current EPA online database.

Table 1: Occupational limits of silver: the permissible exposure limit (PEL) by Occupational Safety and Health Administration (OSHA), the recommended exposure limit (REL) by the National Institute for Occupational Safety and Health (NIOSH), the threshold limit value (TLV) by the American Conference for Governmental Industrial Hygienists (ACGIH), and the primary and secondary maximum contaminant levels, MCL and SMCL respectively, by the U.S. Environmental Protection Agency (EPA).

Occupational Limit Category	**Occupational Limit Type and Organization**

Occupational workplace limits for soluble Ag in air (OSHA) [36a, 37]	0.01 mg m^{-3} (PEL by OSHA and REL by NIOSH)	0.01 mg m^{-3} (TLV by ACGIH, 1980)
Occupational workplace limits of metallic Ag in air (OSHA) [36a, 37]	0.01 mg m^{-3} (PEL by OSHA and REL by NIOSH)	0.1 mg m^{-3} (TLV by ACGIH, 1980)
Minimum regulatory levels in water [36a]	MCL–0.09 μg mL^{-1} (EPA)	SMCL–0.05 μg mL^{-1} (EPA, FDA)
Drinking water standard for select inorganic species in water supplies [38]	N.A. (MCL by EPA, 2002)	100 μg L^{-1} (SMCL by EPA, 2002)
Water quality criteria [39]	Salt water–1.9 μg L^{-1} (EPA)	Fresh water–3.4 μg L^{-1} (EPA)
ACGIH [37]	Metallic–100 μg L^{-1}	Soluble–10 μg L^{-1}

Due to its application, nanotechnology crosses paths with the transport and fate of NMs in subsurface water. AgNMs may leach in both ionic and particulate forms, potentially entering the freshwater ecosystems [14]. In 1978, the total U.S. loss of Ag to the environment was estimated at 2,470 metric tons [30], and the total U.S. annual anthropogenic release of Ag was approximated at 77,700 kg, 125,000 kg, and 1.01 million kg in air, water, and soil respectively [36a]. In 2007, the yearly worldwide production of Ag reached 28,000 metric tons [40], out of which AgNMs constituted approximately 1.78% [41]. Recently, AgNPs were found to leach variably from antibacterial products, such as socks [41] and textiles (approximately 0–377 μg g^{-1}), and exterior paints by dissolution and weathering, respectively [14]. Compared to micro-sized Ag, nano-sized Ag can more readily release Ag^{+} under

acidic conditions (pH~0.5), for example in sulfuric geysers or following acid mine drainage [14]. AgNM toxicity to organisms is expected to increase with release of Ag^+, which occurs when AgNMs undergo physical, microbiological, and chemical transformations [14, 35] and for small size NPs (< 20 nm) [42]. Due to limited empirical data, probabilistic analysis and Monte Carlo simulations, employed in predicting the environmental release of AgNPs, produced a risk quotient larger than one, which raises concerns for freshwater ecosystems and aquatic sediments [14].

1.2.2. TOXICITY OF SILVER:

Interaction of NMs with certain biological matrices has indicated adverse effects. Cytotoxicity of AgNPs [43] has been studied and compared for viruses [7], bacteria [6, 17] including fish [18] and plant [44] pathogens, and spores [17]) and fungi [6]. Surface charge-dependent toxicity of AgNPs was studied on *Bacillu*s species under aerobic conditions [45]. At basal pH, bacteria with negative cell surface charge were observed to complex with the metal and to alter their protein structure [29]. Cell damage was found to be neurotoxicological (*e.g.*, impairment of the blood-brain barrier function with a continued neurotoxic effect upon Ag treatment [46]), genotoxic (*e.g.*, mitosis disruption [47], DNA fragmentation [26]) or oxidative (*e.g.*, increase in lipid peroxidation caused by ROS [26]). AgNP toxicity varied with NP shape [48], size [49], treatment dose [26], and surface reactivity (hydrophobicity) [14], which can be tuned by surface functionalization [13] for subcellular placement at molecular level [25]. Bacterial resistance [14] to Ag has been reported since 1975 with little mechanistic explanations [50]. This highlights the importance of compatibility

for targeting different applications. With scrutiny, the antimicrobial activity of AgNPs has been attributed to the timely release of ionic silver (Ag^+), which occurs by oxidation of metallic silver [14, 42, 51] or when colloidal stability is weakened and electrostatic repulsion forces can no longer prevent aggregation in either a polar suspension or powder form [51]. Silver's ionization potentials allow the release of Ag^+, which induce the formation of free radicals or ROS, and subsequently exert cellular oxidative stress [52]. Ag^+ was found to be released at oxidized, convex AgNP surfaces smaller than 10 nm in diameter. Less Ag^+ is released for larger size AgNPs, indicating the role of the nanosize area on the AgNP toxicity [53a]. Liu *et al.* confirmed that the release of Ag^+ ions may be stimulated by processes such as pre-oxidation, particle size reduction [53b] or experimental conditions, such as temperature increase (0-37 ˚C) and pH decrease [53c]. In contrast, the release of Ag^+ may be inhibited by "thiol and citrate binding, formation of sulfidic coatings, or the scavenging of peroxy-intermediates" [53b]. The addition of natural organic matter (NOM) such as humic and fulvic acids, which are commonly found in groundwater and soil, may also decrease the release rate of Ag^+. These Ag^+ ions may adsorb to the AgNP surface resulting in three forms of colloidal silver: Ag^0 solids, free Ag^+ ions or (AgNP) complexed Ag^+ species [53c].

1.2.3. TRANSPORT AND FATE OF SILVER THROUGH GROUND WATER AND SOIL:

Environmental Mobility of NMs

The accumulation of a contaminant in an ecosystem highly depends on the environment. The diversity of subsurface water alters the mobility of a colloid through various saturation and porosity levels of the geologic media [54]. The water table is a diverse compartment that acts as a boundary between the **saturated (ground water)** and unsaturated (vadose) zones of the subsurface [55]. The aqueous content of soil impacts factors like pH, osmotic pressure, aeration and solubility. Additional parameters such as moisture content (water to total volume ratio), porosity (void to total volume ratio), and saturation (water to void volume ratio) can affect the attachment or sorption of contaminants to the media. Compared to hydrophobic colloids, hydrophilic NMs are more easily remediated (*i.e.*, removed from saturated zones by pump-and-treat methods), though they can also migrate further through the subsurface by advective flow reaching ground water [54]. Compared to sea or surface water, ground water moves slowly, has a relatively stable temperature, low turbidity, high mineral content, richness in divalent iron and magnesium ions, dissolved carbon dioxide, dihydrogen sulfide (which helps breaking down organic matter), ammonium, nitrates, silica, chlorinated solvents and iron-feeding bacteria. It is often low in dissolved oxygen and microbiologically pure. Water flow is controlled by permeability of the geologic media [56].

"Waterborne nanoparticles generally settle more slowly than larger particles of the same material" [1]. However, they tend to adsorb onto sediments and soil due to their high surface area to mass ratios and reactivity, potentially facilitating their removal as sorbed material from water columns by filtration [1]. **Surface functionalization** of NMs affects the extent at which they would be retained in

porous matrices and subsequently their mobility [14]. Colloidal NPs may also become more stable [29] within the soil upon binding organic ligands [14, 29], which may increase their mobility [14]. Upon biotic (*e.g.*, anaerobic reduction under benthic conditions) or abiotic (*e.g.*, hydrolysis, photo catalysis) degradation, NP properties may also change [1]. Stable NPs such as silicon dioxide (SiO_2) can easily spread within aquatic environments. However, their aquatic dispersal may be limited by their polymer bridging or chain entanglement with fibrillar natural organic matter (NOM), *e.g.*, polysaccharides and glycoproteins [14]. Such factors, including salinity, may enhance NP sedimentation and exposure to benthic communities [14]. In fresh water, NM colloids may be stabilized by contact with NOMs like humic acid, which may coat the NM surface with a negatively charged layer [57, 58, 59]. Complexation with NOMs can promote the breakdown of metallic NMs in anaerobic sediments [1]. It should be noted that silver may be present in sulfide and chloride complexes, NOM, dissolved organic carbon, and colloidal suspensions [35]. Similarly, colloidal AgNPs may facilitate or interfere with the transport of other contaminants. For example, nanosilver stability was shown to increase in the presence of NOMs but to decrease at high ionic strength [60]. NPs may also sequester soil minerals of opposite charge through electrostatic interactions. Reductive dehalogenation by AgNPs was found to produce an insoluble salt and a less toxic hydrocarbon [20, 29].

1.2.4. TRANSPORT MECHANISMS OF SOLUTES IN POROUS, SATURATED MEDIA:

Advection-Dispersion

Transport mechanisms have been proposed in the form of filtration assessment for solutes [54] and colloidal particles in porous media [61, 62]. Starting at a source, a contaminant (*e.g.*, AgNPs) or solute migrates in the direction of aqueous flow by the process of **advection**. The contaminant may also spread due to variations in velocity through the process known as **dispersion**. Therefore, transport of a solute in ground water and soil is often simulated using an **advection-dispersion** model [54, 64]. As the solute moves farther from the source point, it creates a plume in the form of concentric layers with decreasing concentration gradient [54]. Solute transport in the aqueous phase of the subsurface abides by physical (dispersion-advection and straining) as well as chemical (phase partitioning, degradation, and electrostatic and London Van der Waal interactions) forces [14, 54, 63, 64].

To represent solute transport through saturated, porous media, *i.e.*, filter bed, **breakthrough curves (BTC)** are plotted as a retained or recovered quantifiable amount against a constantly varying parameter (*e.g.*, adsorbed volume against pressure or percent settled volume against pH) [62]. In this study, concentration will be plotted against time, which will be a constantly varying parameter.

Classical Filtration Theory (CFT)

Classical Filtration theory (CFT) describes physical mechanisms for the removal or capture of suspended particles larger than 1 μm by water-saturated porous media, designated as the filter bed or collector [62]. CFT describes the

following transport mechanisms in water: a) **sedimentation** (for a particle which has density [64] larger than that of liquid and which deviates in its path due to its "buoyant weight" and the "fluid drag" it is subjected to), b) **settling and interception** (for a particle traveling in a fluid phase with a direction driven by gravitational impact, which may leave the path of its bulk flow upon contact with the grain pores of the collector), and c) **diffusion** (for particles that collide via Brownian motion, usually significant for particles smaller than 1 μm) [61, 62, 64] d) **inertial impaction** (for a particle that deviates from its path by colliding with the collector media due to the inertia driving it) [61]. Larger particles may coagulate with other particles and may be captured due to the "velocity gradients" and "fluid motion" [62]. Surface charge [54, 64] and size of particles as well as their flow rate [new ref 62] are especially important in the transport of colloidal NPs.

Non-Equilibrium Sorption

It is expected that the transport of a solute would exhibit a combination of reversible and irreversible sorption (attachment/detachment) to the media. Reversible attachment may be relatively fast or slow in comparison with other transport timescales. If fast, attachment and detachment may be modeled as an equilibrium process. If slow, attachment and detachment are said to be rate-limited [54]. Rate-limited or non-equilibrium attachment/detachment is indicated by a **breakthrough curve** (BTC), where low concentrations of NPs persist for relatively long periods. However, if a large portion of AgNPs is variably strained, dispersed or irreversibly attached to the media, the breakthrough pattern will deviate from the symmetrical sharp curve, indicating a **non-equilibrium** sorption and a **rate-limited**

mass transfer [54]. Irreversible and reversible capture (either rate-limited or equilibrium) may be combined into the advection-dispersion model [54] to simulate transport of NPs in porous media [62]. For this purpose, the dependence of sorption on rate or equilibrium can be depicted through models, such as rate-limited mass transfer, advection-dispersion, and solute transport [54, 63]. CFT explains important mechanisms of capture but does not account for reversible capture of the solute molecules through the media [62].

Deviation from Transport Theory

Deviations from the CFT have been reported for the deposition of microbial particles in granular clean beds [65]. These deviations were related to the heterogeneity in microbial surface properties, distributions in the interaction energies between particles, charge heterogeneity at the media surface, and deposition dynamics [65]. Kinetics were found to depend on chemical heterogeneity, rather than spatial distribution or average charge [65]. Tufenkji *et al.* found that the CFT deviations can occur when both unfavorable (repulsive forces) and favorable conditions affect the deposition of polystyrene microspheres [63]. The rate of deposition was affected by the repulsive energy barrier and the primary and secondary energy minima [65]. Slow deposition is characteristic to particles that cannot overcome the repulsive energy barrier; whereas particles that overcome it can reach the primary energy minimum [65].

Previous studies of Nanoparticle (NP) Transport

Previous studies have examined the transport of NPs in one-dimensional, porous saturated systems [45], simulating the ground water flow. For example, in the case of transported single walled carbon nanotubes (0.02−21.4 μm in length), mass was retained throughout the entire depth, while larger bundles of carbon nanotubes were collected near the inlet of the column [66]. Raychoudhury *et al.* performed a downward transport of nano-zerovalent iron (NZVI) coated with carboxy methylcellulose (CMC-NZVI) with a TEM diameter of 85 nm, at following conditions: various sizes of porous media (150-755 μm diameter of silica sand) and various NZVI concentrations (85-1700 mg L^{-1} of Fe in 0.1 mM $NaHCO_3$), and low ionic strength (20 mg L^{-1} of KNO_3^{-1}) [67]. In contrast with CFT predictions [62], they reported both reversible and irreversible capture of the NZVI through sand. This study also reported that the straining rate was affected by the relative size of NZVI with respect to the media [67]. The retention of the CMC-NZVI was also observed at the inlet and in the case of the finer media at low ionic strength; it was attributed to straining and wedging of the NPs. The straining rate was also affected by the relative size of nZVI with respect to the media [67].

El Badawy *et al.* [68] compared the upflow transport of four types of coated and uncoated AgNPs through three types of porous media saturated with a KBr solution (10 ppm of Br^-). The four types of AgNPs were 1) electrostatically-stabilized, uncoated H_2-AgNPs, 2) electrostatically stabilized, citrate-coated AgNPs, 3) sterically-stabilized, polyvinylpyrrolidone-coated AgNPs, and 4) electro-sterically-stabilized, polyethyleneimine-coated AgNPs. The transport experiments were carried out at a column length of 10 cm, a pH value of 7.0, and a

fixed flow rate of 1.0 mL min^{-1}. The three porous sand media were represented by 1) quartz sand, 2) ferrihydrite-coated sand, and 3) kaolin-coated sand. The citrate-stabilized AgNPs, which are negatively charged similarly to the borohydride-stabilized AgNPs in this project, exhibited a more facilitated mobility, lower retention and lower deposition in quartz sand in comparison to the other two media. The quartz sand grains had an average diameter of 360 μm, which is close to the media diameter range of this study (400-600 μm). Straining was determined to govern the deposition mechanism of the citrate-stabilized AgNPs within the kaolin-coated media [68]. The same research group [69a] evaluated the impact of pH, ionic strength and electrolyte type on the same four types of AgNPs in addition to the borohydride-coated AgNPs (*i.e.*, the Creighton AgNPs). It was found that the uncoated H_2-AgNPs, the citrate- and borohydride-coated AgNPs aggregated at high ionic strength (100 mM of $NaNO_3$), very acidic conditions (pH of 3.0), and in the presence of divalent cations (Ca^{2+}). The same factors had minimal impact on the sterically-stabilized AgNPs, while only the pH affected the surface charge and aggregation of the electro-sterically-stabilized AgNPs. A recent study by Lin *et al.*[70a] investigated the deposition of borohydride-reduced AgNPs (12 nm average TEM diameter) in two geochemical porous media, namely uncoated and hematite-coated spherical silicate glass beads (300 − 400 μm in diameter, saturated by $NaNO_3$), and a mixture of the two at different mass ratios. A higher affinity of AgNPs was observed for the hematite-coated glass beads in good agreement with the coated-media from the El Badawy *et al.*'s studies [68]. Therefore, we anticipate obtaining **facilitated transport** in our study for the unmodified glass beads as in

these two studies. The reported adsorption profiles indicated that the concentration of AgNPs in the effluent increased and reached a plateau upon continuous injection, as predicted by the classical filtration theory [70a]. Furthermore, the volume of tracer ions was found to be much larger than that of the stock Creighton colloid, and it was concluded that the residual ions present in the colloidal samples of AgNPs (*e.g.*, excess reagent, byproduct and Ag^+ ions) contributed to a very small degree to the total ionic strength [70a].

Project Significance

To the best of our knowledge, no transport studies through porous saturated media in **one-dimensional** column systems were reported for **electrostatically-stabilized, borohydride-reduced colloids** (*i.e.*, Creighton colloids) as a function of AgNP size, under fixed pH and ionic strength conditions. In light of the increased release of AgNPs into subsurface water systems, the study of AgNP mobility as a function of their size would provide insight for risk assessment. The transport mechanism and fate of AgNPs may be determined starting with a simple and finite 1-D transport model through silica beads as porous media. Known as quartz, crystalline silica or silicate, silicon dioxide (SiO_2) is present in many industrial uses and pharmaceutical products. A recent, comprehensive review [42] indicated that colloidal AgNPs are most commonly synthesized by the chemical reduction of silver nitrate (> 80% of the published articles) with sodium borohydride (Creighton - 23%) or sodium citrate (Lee-Meisel - 10%) in water solvent (> 80%).

Furthermore, sodium citrate was not identified as an immediate, major environmental risk factor [42]. Such types of bottom-up fabrication methods are more often utilized than the top-down methods (< 4%). Creighton colloidal AgNPs are not only widely-used in environmental and toxicological studies but also easily accessible, manufactured, and size selected at copious volumes in a laboratory setup [42, 82, 83].

The synthesis of original Creighton AgNP colloid by reduction of silver nitrate with sodium borohydride yields negatively charged spherical particles, a size distribution of 1-100 nm and a theoretical yield of 15.42 µg mL^{-1}. Its filtration and size selection yields size distribution of 1-20 nm and 50-100 nm in diameter and similar surface plasmon resonance (SPR) profiles for AgNPs. In this study, the analyte (AgNPs) was vertically injected into a **1-D column** filled with a **porous silica** (SiO_2) material and AgNP concentration was measured at the outlet as a function of time [54] in order to produce the **breakthrough curve**. Targeted conditions included: influent concentrations of AgNPs of 15.3 mg L^{-1} and KCl of 133 mg L^{-1}, flow rate of 1.0 mL min^{-1}, and a fixed pH of 7.8. The pH was measured under the experimental conditions and was not modified. The selection of the moderate pH and the low ionic strength would help simulate aqueous flow through **subsurface water** systems and allow AgNPs to remain stable and prevent acidic degradation or aggregation. With the purpose of modeling AgNPs as a potential environmental contaminant, the AgNPs Creighton colloid was injected through the column as synthesized and its concentration is approximately 150-fold larger than the U.S. EPA SMCL of 0.1 mg L^{-1} [36b]. The experiment was conducted at two flow

rates (1.0 and 2.0 mL min^{-1}), which have been used in previous studies and are low enough for extrapolation to realistic transport while overcoming practical limitations, such as straining of injected NPs [67], for experimental purposes [68]. The filtration and size selection would result in a **50 nm concentrate** (also known as the first retentate in TFF with an expected average concentration of ~ 600-700 μg mL^{-1}, and size range 20-100 nm) and a **100 kD retentate** (which is expected to have a size distribution of 1-20 nm, average size of about 9-11 nm and concentration of about 4000-10,000 μg mL^{-1} [82, 84a] (as determined by previous studies). The retentates are about 50- and 500-fold more concentrated than the original colloid respectively. The retentates have more homogeneous size distribution with moderate NP aggregation and minimal byproducts [82, 83] as compared to the original colloid, since filtration eliminates excess reagents. The variation in size would allow to examine AgNP mobility as a function of average diameter, size distribution, concentration, and purity [82, 83].

1.3. HYPOTHESIS

It is hypothesized that the **size** and **flow rate** of Creighton colloidal silver nanoparticles (AgNPs), which are pulse-injected through a confined, saturated, porous, one-dimensional column simulating the groundwater-soil flow, will affect the concentration breakthrough curves (BTC) of AgNPs. It is expected that:

(1) The Creighton AgNPs will experience attachment to the porous media surface followed by detachment and elution from the column (*i.e.*, partial **reversible**

capture) probably due to electrostatic interactions between the silica and the negative AgNP surface. The portion of transported AgNPs that attach irreversibly onto the media will result in a **mass loss**, which is expected to increase with the increase in AgNP size.

(2) The smaller **size** AgNPs (1-20 nm in diameter) will travel faster through the 1-D column (*i.e.*, enhanced mobility) compared to the larger size AgNPs (50-100 nm or 1-100 nm) perhaps due to their larger surface area to volume ratio.

(3) The **breakthrough pattern** will exhibit a rate-limited, non-equilibrium pattern with respect to the selected experimental moderate flow rates simulating ground water flow, probably due to varying attachment/detachment kinetics of AgNP colloid and the varying AgNP size and surface charge.

1.4. SPECIFIC AIMS

1. To synthesize and characterize a large volume of Creighton colloidal AgNPs (15.40 μg mL^{-1} of silver) of moderate size distribution (1−100 nm) and stability (pH 7.8);
2. To examine the fate and transport of Creighton colloidal AgNPs (1-20 nm, 50-100 nm, and 1-100 nm in diameter) through saturated, porous media at fixed ionic strength (0.01 mM of KCl) and flow rates (1 and 2 mL min^{-1});
3. To implement the newly developed standard operating procedure for the ICP-OES-based quantification of Ag within the Creighton colloidal AgNP samples into an instrumental analysis laboratory experiment for undergraduate students.

2. TECHNICAL APPROACH

SPECIFIC AIM 1

2.1. SYNTHESIS AND SIZE SELECTION OF SILVER NANOPARTICLES (AGNPS)

2.1.1. NANOPARTICLE SYNTHESIS BACKGROUND:

Nanofabrication of powders, solids, or suspensions employs a variety of bottom-up (*e.g.*, chemical precipitation and gas phase agglomeration [70b]) and top-down (*e.g.*, attrition [70b] and electron beam or "Dip-Pen" nanolithography [69]) approaches [42]. The former involves soft matter [71] and assembly of molecular or atomic structures in a liquid phase [69b]. In a liquid phase self-assembly, formation of nuclei is initiated so that AgNP diameter and size distribution are easily controlled by varying their growth rate kinetically and/or thermodynamically, and selecting proper temperature, pH and solvent concentration [72]. The top-down approach involves patterning of large surfaces while easily controlling shape, size and orientation [69b] but risking structural imperfections [70b]. Synthesis targets uniform chemical composition, size, shape or morphology, crystal structure, and dispersion within the matrix [71]. Basic physical synthesis includes methods such as evaporation-condensation in a tube furnace, laser ablation, and photo-induced synthesis. Chemical methods include template methods, micro-emulsion, and chemical reduction with citrate, borohydride, ascorbate,

al hydrogen or other agents, yielding colloidal AgNPs in an aqueous suspension [72]. Green synthesis has been explored for silver and gold using bacteria [29] and fungi [73] to biosorb [74] and reduce the noble metal salt, yielding a well-defined size (as low as 15 nm) and distinct morphology that compete with other methods.

The Creighton method, used in this study, employs a stepwise dimerization and nucleus growth by the gradual addition of silver atoms. Sodium borohydrate is converted into boric acid, $B(OH)_3$, upon contact with water. Sodium hydroxide, NaOH, performs a nucleophilic attack on one hydrogen atom to facilitate placement of the hydroxide group. Creighton colloidal AgNPs were found to be round, negatively charged (with expected Zeta potential for $AgNPs^-$ at 6.8 pH according to a previous study [84b]) and to have a moderate size distribution, with an average diameter of ~ 10–11 nm [74, 75]. Aggregation of suspended AgNPs is attributed to the presence of certain organic materials and steric or electrostatic repulsions [67] within the sol. Aggregation of Creighton AgNPs is minimized through electrostatic interactions, maintained by an electrical layering between the metal nanoparticles and surrounding anions in the sol [75, 76].

2.1.2. SYNTHESIS OF CREIGHTON SILVER NANOPARTICLES:

A slightly modified [75] Creighton [74] method was employed for the fabrication of AgNPs through the reduction of silver nitrate aqueous solution ($AgNO_3$, Fisher Scientific, prepared from 1.7 mg in 10 mL of water) with sodium borodydride ($NaBH_4$, Fisher Scientific, prepared from 4.53 mg in 60 mL of water)

using a 1 to 2 mM ratio. $NaBH_4$ was stored in a desiccator and flushed with inert gas before use. The two-hour, dropwise (1 drop per second) titration reaction (Figure 1) at 4±2 °C produced a highly pure, colloidal suspension (Figure 1) with minimal byproducts [77], an optimized yield (theoretical yield of 15.42 µg mL^{-1}) of nanosilver, and increased stability (shelf life of 6–12 months). Adequate control of temperature, light, and sterile conditions prevented hydrolysis of $NaBH_4$ and photodecomposition of $AgNO_3$ [75]. The colloid was stored at 4±2 °C in a pre-cleaned Amber bottle until further use.

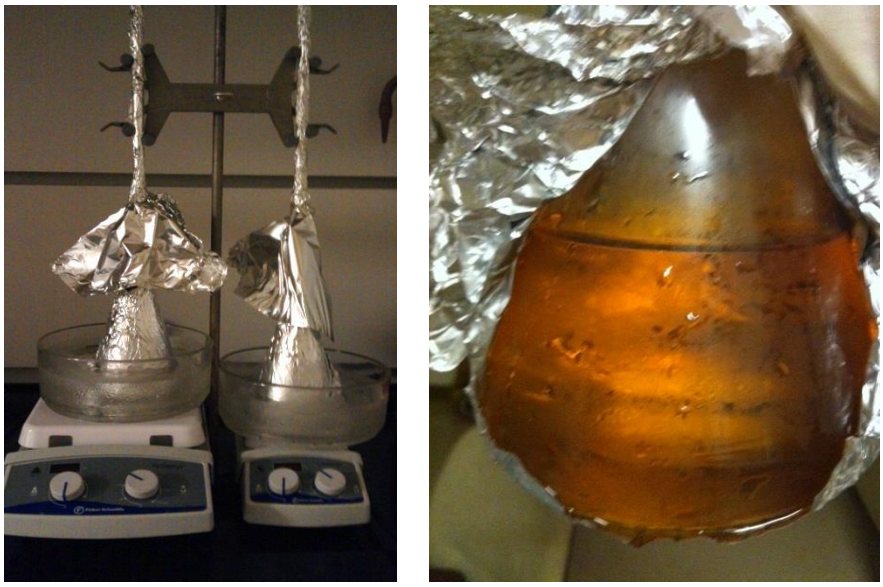

Figure 1. **Left**: Controlled titration setup for the Creighton synthesis. **Right**: A yellow Creighton colloid of AgNPs produced through the titration reaction.

2.1.3. TANGENTIAL FLOW FILTRATION (TFF) OF SILVER NANOPARTICLES:

Working Principle

Tangential flow filtration (TFF) is a membrane-based separation method of solutes or particulates in a biological, environmental, or chemical liquid sample, including aqueous colloidal NPs in a suspension. TFF may be utilized for the size selection, concentration, and purification of micro or nano (1 kD–1000 kD) scale components based on their size and charge [78]. Polysulfone and cellulose are commonly used in TFF fiber membranes [79]. In TFF, the sample fluid is fed tangentially across a membrane surface of a specific pore size, where it experiences a slowly declining flux rate during the size-selection process. In contrast to dead-end filtration, this tangential flow geometry prevents the build-up of NPs at the membrane surface. The particles smaller than the pore size pass through the membrane (*i.e.*, filtrate), while the larger ones are held upstream (*i.e.*, retentate or concentrate) [78]. The retentate is later collected at the membrane port, while the filtrate may be recirculated to achieve the desired volume concentration and purification [80]. Crossflow velocity and transmembrane pressure are created by a negative pressure between the feed and the retentate port [80]. Successful TFF has been accomplished in our previous studies, specifically for Creighton AgNPs [81, 82].

Operating Conditions

In this experiment, a three-step TFF process (Figure 3) was employed to "green" size-select, concentrate, and purify a large volume of Creighton colloidal AgNPs (4.0 L, 1–100 nm in diameter, and ~15 mg L^{-1} of Ag). At each step, the TFF system (a KrosFlo II system by Spectrum Laboratories) was assembled using one of three Polyethersulfone (PES) membrane (Spectrum Labs MidiKros® Hollow

Fiber Module (P-X3-010E-300-02N)) filters of pore sizes of 50 nm, 100 kD, and 100 kD and surface areas (SA) of 460 cm^2, 200 cm^2, and 20 cm^2, respectively (Figure 2). Equipment also included Teflon tubing segments (sizes 14, 17, and 24, Masterflex® C-Flex®), a pressure gauge at the feed controlled by a peristaltic pump (Masterflex®), clamps, and sample reservoirs (Figure 3).

Before assembly of the TFF system (Figure 3), tubing and filters were rinsed with 2% nitric acid and high-purity water to remove previously strained particles. Upon the system assembly at each step, the corresponding tubing size was selected in the pump settings. Vertical exiting ports were positioned below the entrance ports to prevent back flow. The feed was carried into the pump and then the filter (entrance and exit ports) via the segment tubing, while the retentate port was closed on the filter. Recirculation of the retentate with the remaining feed was allowed by a Y-splitter placed between the retentate port, the pump, and the feed reservoir. Between the exit port and the Y-splitter, a T-splitter was secured to further control the recirculation and collection of the retentate. All tubing junctions and ports were secured with zip-ties to prevent leakage. Each filter module was mounted vertically with the support of one stand and a three-prong clamp at each of its ends. Figure 2 shows the schematic of the three-step TFU process with the two final products highlighted in blue.

In the first step, the original AgNP colloid was fed through the size 17 Masterflex® C-Flex® tubing into the MidiKros® 50-nm filter at gradually increasing pump rates from 250–350 to 650–750 mL min^{-1} and was continuously circulated until the reservoir became void of AgNPs. An approximate volume of 50

mL of the size-selected and concentrated retentate (denoted as 50 cc) was collected at the T-valve. This is the first main filtration product that contains AgNPs larger than 50 nm in diameter and an approximate concentration of 1,000 μg mL^{-1}. The filtrate (denoted as 50 f) was collected at the exiting port of the filter module and preserved for the next step.

In the second step, the 50-nm filtrate (50 f) was further size-selected using the size 24 Masterflex® C-Flex® and the 100-kD MidiKros® filter. This significantly concentrated the filtrate into an approximate volume of 50 mL of dark brown retentate product, which is the first 100 kD retentate product. The filtrate from this step was discarded appropriately.

In the third step, the first 100 kD retentate from the second step was further concentrated using the size 14 Masterflex® C-Flex® tubing and the 100-kD MicroKros® filter. The filtration was started at a pump rate of 25–35 mL min^{-1}, gradually increased to 85–95 mL min^{-1} and continued until the retentate volume in the reservoir became minimal. The remainder concentrated volume of approximately 4–6 mL was transferred from the tubing and filter into the reservoir container and collected. This is the second main filtration product (denoted as 100 cc) that contains AgNPs smaller than 20 nm of an approximate concentration of 10,000 μg mL^{-1}.

Once the TFF process was completed, the pump was turned off and the system disassembled. The filters were cleaned and stored in a 2-5% nitric acid solution to maintain the membrane dignity. The products were then characterized

and employed in the transport experiments (see Specific Aim 2, section 2.2.) within 5 days of TFF processing to prevent AgNP aggregation.

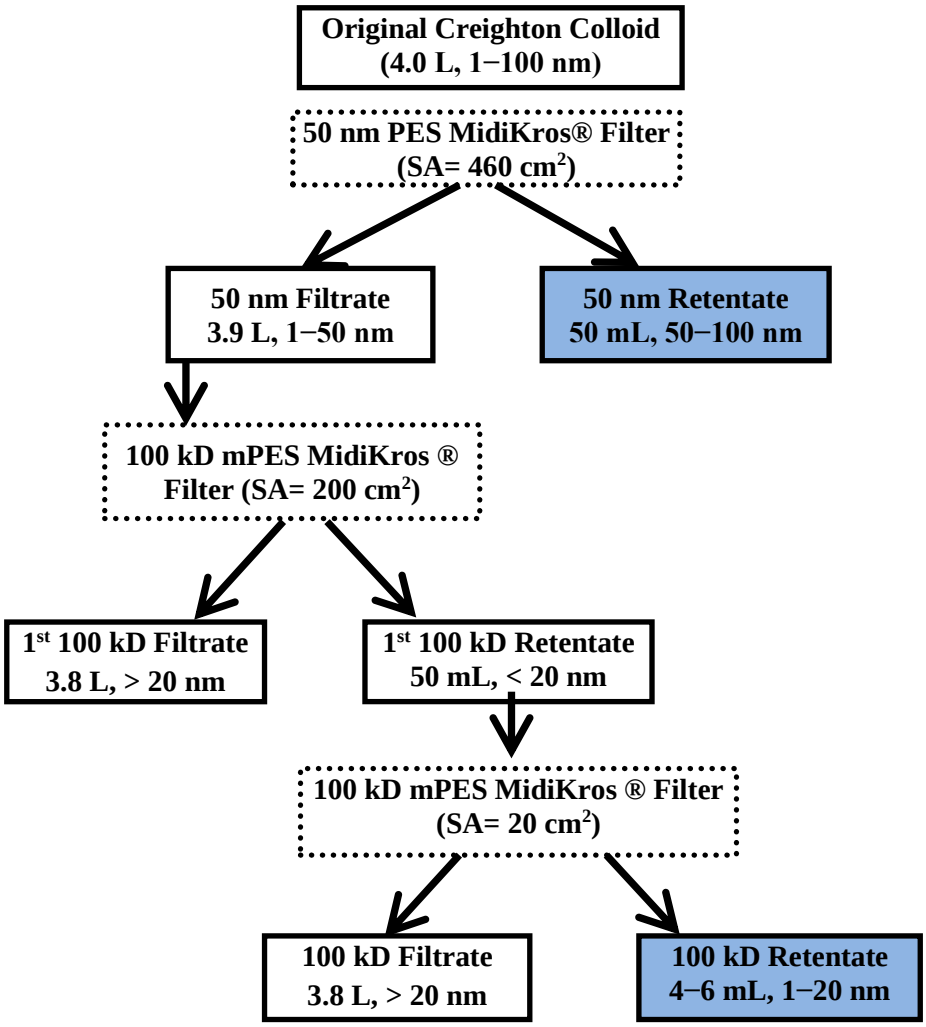

Figure 2: Diagram of the three-step TFF filtration process. The properties of the hollow fiber membrane filters (pore size, composition, manufacturer, and surface area) and the filtration products (approximate volumes and projected size ranges) are indicated.

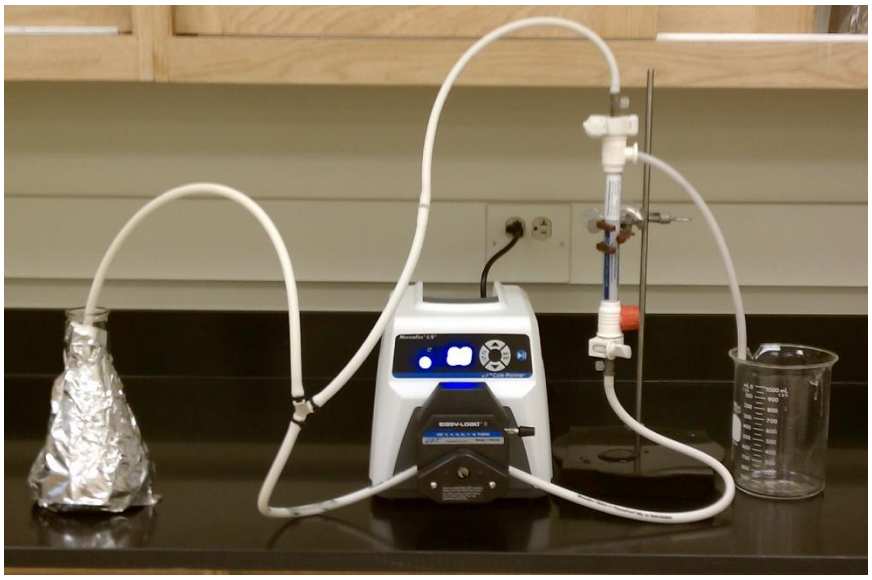

Figure 3: Photograph of the home-built tangential flow filtration (TFF) system showing: the peristaltic pump (Masterflex) connected to the Y-junction within the tubing segment between the reservoir and the filter, and the first 100 kD filter mounted vertically at the right side of the pump (Dr. Pavel Sizemore's lab, 214 Oelman Hall).

2.2. CHARACTERIZATION OF SILVER NANOPARTICLES

The physicochemical properties of all representative TFF-colloidal samples of AgNPs were characterized following six of the nine standards as recommended by the U.S EPA: **average size, size distribution, shape, solubility, surface charge, and concentration** [7, 83].

2.2.1. CHARACTERIZATION BY ULTRAVIOLET-VISIBLE ABSORPTION SPECTROPHOTOMETRY:

Working Principle

Ultraviolet-Visible (UV-Vis) absorption spectrophotometry allows detection of quantized excitation of certain electronic states followed by subsequent rotations, vibrations, or oscillations within molecular species that absorb light between 200 and 1100 nm, yielding a quantifiable wavelength-specific absorption. UV-Vis absorption spectrophotometry facilitates the rough estimation of the shape, size, and aggregation (polydispersity) state of Creighton colloidal AgNPs through their surface plasmon resonance (SPR) peak profile. The Lambert Beer law (Equation 1) relates the absorbance (*A*) to the concentration of AgNPs in the colloidal samples (*c*) and the molar absorptivity of the characteristic electron oscillation (ϵ) [85].

$$A = \epsilon bc = log\left(\frac{P_0}{P}\right) \qquad \text{Equation 1}$$

Absorbed energy is thus measured as the amount of photons in the cuvette path length area by difference to the transmittance, which is expressed as the logarithmic ratio of the power lost in the final transmitted beam (*P*) compared to the incident beam (P_0) [85]. It should be noted that linearity between the absorbance and concentration may be hindered for certain AgNPs due to deviations in the molar absorptivity (*i.e.*, at high concentration or for variable refractive indices) and the effect of polychromatic absorbance, which may be caused by the nano-dimension behavior [85], occurring for different NP size [13].

Sample Preparation

Freshly synthesized AgNP samples were used after 8 to 24 hours following synthesis or elution from the column system (Aim 3, section 2.2). An aliquot of each original colloid sample was transferred to a 1 mL disposable cuvette and quantitatively diluted with water in a 1 to 10 volume ratio (V:V) [75, 86]. The influent and effluent samples collected from the transport experiments (Aim 3) were not diluted.

Operating Conditions

In this study, UV-Vis absorption spectra were acquired using a dual beam *Cary 50 Bio* spectrophotometer (by Varian Inc.) equipped with a mercury lamp (emission of 254 nm), a Xenon flash lamp module (80 Hz, 12.5 ms measurement intervals), a focusing mirror, a beam splitter, a cuvette flow cell, a fast scanning *Czerny-Turner* monochromator (0.28 m, 24,000 nm per minute capacity), and a dual silicon diode set of detectors. Operating conditions included: range of 190–1100 nm, dual beam laser mode, fast monochromator scan rate of 4800 nm min^{-1} and spectral intervals of 1 nm. A blank cuvette of water was used to calibrate absorbance to a zero baseline prior to each run.

2.2.2. CHARACTERIZATION BY MICRO-RAMAN SPECTROSCOPY:

Working Principle

Inelastic Raman scattering is based on irradiating a molecule with a monochromatic laser beam (in the visible, near infrared, or ultraviolet spectral

range), and exciting it into a virtual state [85, 87]. The molecule then relaxes to a vibrational state that is different than its original state by emitting a photon of lower (Antistokes) or higher (Stokes) energy than that of the incident monochromatic source. The energy difference between the original and final vibrational states of a molecule is translated into a frequency shift specific to the molecule's chemical structure [87].

Sample Preparation

Samples were directly placed into 3 mL quartz cuvettes and used with no further preparation.

Operating Conditions

In this study, the Raman spectra of the colloidal samples of AgNPs were collected in a 3 mL quartz cuvette using a micro-Raman LabRAM 800HR system (HORIBA Jobin Yvon Inc.). The Raman system was equipped with a confocal microscope, a sample illumination system, a He-Ne excitation laser (20 mW output), light collection optics, a wavelength selector (notch filter), a CCD detector (1024x526 pixels), and a 800 mm focal length spectrograph having a kinematic grating and laser diode alignment. Operating conditions included a spectral range from 100 to 4000 cm^{-1}, an excitation wavelength of 632.8 nm (HeNe laser), a holographic grating of 600 grooves/mm, a confocal hole of 300 µm, accumulation cycles of 5, and an acquisition time of 30 s.

2.2.3. CHARACTERIZATION BY TRANSMISSION ELECTRON MICROSCOPY:

Working Principle

Transmission electron microscopy (TEM) is a powerful tool for the accurate determination of the average size, size distribution, and a pseudo three-dimensional shape presentation of a fixed NP suspension. In TEM, an electron beam of an extremely short wavelength is focused and magnified through a series of magnetic lenses (two condenser lenses and one condenser aperture) before it interacts normally with a cooled, thin sample layer (< 100 nm) under high vacuum and high accelerating voltage conditions. A transmitted beam forms from electrons that are elastically scattered off the thin, dehydrated sample. It is then passed through two apertures and another set of three magnifying lenses to produce a photograph that is saved as a .jpg or .tif image [89].

Sample Preparation

A 20 μL volume per colloidal AgNP sample was carefully deposited on a 300-mesh (3.0 mm) formvar-coated copper grid and allowed to dry in a desiccator completely before measurement [76].

Operating Conditions

In this study, TEM images of AgNPs were recorded with a high resolution (HR) TEM (Hitachi, H-7600) that is equipped with an AMT digital CCD system.

Operating conditions were controlled through the Windows R2000 OS30 computer software: high contrast (x700–x600,000 magnification), high resolution (x1,000–x600,000 magnification), accelerating beam of 100–120 kV, point-to-point resolution of 0.36 nm and crystal lattice at 0.204 nm [88]. The settings included 20 nm resolution, 200,000x magnification, and 120 kV for the original Creighton colloid and the 100 kD retentate, and 20 nm resolution, 200,000x magnification and 70.0 kV for the 50 nm retentate.

Acquired tagged image files (.tif) were processed in the *Image J* software. An area threshold limit of 1 nm^2 was applied. Particles outlined by the software were manually affirmed in order to eliminate outlined noises. Single particles were determined as enclosed perimeters that are significantly darker than the background by using automated count settings. TEM size distribution histograms were then constructed in *OriginPro 8.5* software by analyzing at least N = 400 Creighton colloidal AgNPs per histogram.

2.2.4. CHARACTERIZATION BY ABSORPTION AND EMISSION SPECTROSCOPY:

Working Principle of Absorption Spectroscopy

Established in 1860 and intensively applied since 1955, flame atomic absorption spectroscopy (FAAS) allows free atoms in the gas phase to absorb optical radiation as a narrow spectral line, characteristic of the absorbing element.

Quantification is possible through application of the Lambert-Beer law. In FAAS absorbance (A), the negative logarithm of percent transmission is directly proportional to the concentration of the absorbing element (c) and the thickness of the absorbing layer (d), which is determined by the burner head length.

$$A = -\log\left(\frac{\Phi_t(\lambda)}{\Phi_i(\lambda)}\right) = kcd \qquad \textbf{Equation 2}\ [33]$$

In Equation 2, ϕ_t is the power of transmitted radiation, ϕ_i, the power of incident radiation, and *k*, the correlation factor.

A standard FAAS setup consists of a radiation source, an atomizer, a monochromator, a detector, an amplifier, a signal-processing unit and a readout device. The sample is up-taken by an aspirator with a controlled flow to a mixing chamber burner, where it is converted to an aerosol. The aerosolized sample portion is then carried to the nebulizer, which continuously sprays the sample into the burner head, where the flame of air-acetylene is generated. The free atoms in the gas phase are excited when they contact the gas carrier, and they absorb the optical radiation emitted by a cathode or electrodeless discharge lamp. The radiation is spectrally dispersed and the analytical line is isolated by a monochromator. Continuous spectrum sources may be used for background correction. The absorbed radiation is then detected by the photomultiplier tube, which converts the signal into a digital relative quantity. It is then amplified and transmitted to a signal-processing unit and a readout device [85].

For an aspiration rate of 5–10 mL min^{-1}, 1–2 mL of sample per minute are measured. Non spectral interferences are avoided by chemical digestion and by minimizing sample viscosity. Because the matrix in this study was simple (*i.e.*,

AgNP in acidified aqueous matrix), ionization of the analyte was inconsiderable. The formation of refractory gas-phase compounds, which cannot be reversibly dissociated into atoms, was also inconsiderable in the air-acetylene flame [33] for the nanosilver samples.

Sample Preparation for Absorption and Emission Spectroscopy

Calibration standards were prepared using a stock ionic silver solution of 10,000 µg mL^{-1} (Claritas PPT grade, Spex CertiPrep) in 2% nitric acid (HNO_3, 65-70% assay, OPTIMA grade, Fisher Scientific) and ultrapure water (18 MΩ·cm). Calibration blanks, prepared similarly in 2% nitric acid, were analyzed in between samples to avoid carry-over. In this study, effluent and influent samples were chemically digested in nitric acid (2 mL of 70% HNO_3 in a 50 mL sample of Ag) through a cold digestion for 15 minutes followed by a slow boiling digestion (225 °C for about 40 minutes). Digested AgNP samples were then quantitatively diluted in 2% nitric acid and stored at 25˚C.

Operating Conditions for Absorption Spectroscopy

For FAAS, quantification employed an AA240 FS fast sequential FAAS system (Varian Inc.). Samples were measured twice and in triplicate runs. The FAAS operating conditions included: flame (air/acetylene), Ag hollow cathode lamp current (5 mA), wavelength (328.1 nm), slit width (0.7 nm), air flow rate

(13.50 L min^{-1}), acetylene flow rate (2.00 L min^{-1}), acquisition time (3 s), and delay time (3 s).

Operating Conditions for Emission Spectroscopy

For emission spectroscopy analysis, influent and effluent samples were also quantified using a 710 ES ICP-OES instrument (Varian Inc.). A detailed narration of the digestion procedure and the inductively coupled plasma optical emission spectroscopy (ICP-OES) working principle, operating conditions, and calibration methods may be found in section 2.4 or Specific Aim 3.

For each of the FAAS and ICP-OES analyses, the total amount of Ag in the samples was interpolated from the regression analysis of an external calibration and averaged.

2.2.5. CHARACTERIZATION OF ZETA (ζ) POTENTIAL:

Working Principle

The nanoparticle-liquid interface can be described as an electrical double layer with an inner stern layer of closely bound counter ions and an outer diffuse layer governed by weaker forces. Zeta (ζ) potential is the electrokinetic potential [IUPAC reference] that is measured as the potential difference between the dispersion medium and the fluid attached to the colloidal NPs [90a, 90b]. Thus, the Zeta potential may be utilized as an indicator of NP stability in a colloid. The Zeta potential is

determined indirectly by using theoretical models and the electrophoretic mobility of NPs [45, 90a, 90b]. The Zetasizer Nano ZS instrument [90b] used in this study employs the electrophoresis light scattering principle to estimate experimentally the electrophoretic mobility of NPs and therefore describe their surface charge and colloidal stability [45]. An electric field is briefly applied to the aqueous, Creighton colloidal samples between oppositely charged electrodes to measure the AgNP velocities, which are proportional to the magnitude of their Zeta potential. The velocities are estimated from the phase shift of an incident laser beam, which is caused by the NPs moving towards the electrode of opposite charge. This technique, known as Laser Doppler Electrophoresis, [90b], enables the calculation of the Zeta potential distribution from the electrophoretic mobility of NPs using the Smoluchowski theories in conjunction with the dispersant viscosity and the dielectric permittivity [90b].

Sample Preparation

Batches of a concentrated AgNP colloid, namely a 100 kD retentate (100 cc, 1–20 nm in diameter and 65-70 µg mL^{-1} of silver) were treated with 1, 0.1, and 0.01 M of nitric acid (HNO_3, OPTIMA grade, Fisher Scientific) or sodium hydroxide (NaOH, Fisher Scientific) to adjust the pH for Zeta potential measurements. Assigned pH values were recorded using a *Mettler Seven Multi-pH* Meter (Mettler Toledo) at 25 ± 3 °C with buffers of pH 4, 7, and 10 and a calibration slope of -58 – -60 mV/pH.

Operating Conditions

The Zeta potential measurements were performed under the supervision of Dr. Sushil R. Kanel at the Air Force Institute of Technology in the Wright Patterson Air Force Base using a *Zetasizer Nano ZS* instrument (Malvern Instruments Ltd.). The samples were analyzed one time in triplicate measurements using the following operating conditions: a laser source of 633 nm, a detection angle of 173°, a HDD detection range 1 nm−10 μm, ambient temperature, an equilibration time of 1 min, and a pH range of 1–11. It must be noted that Zeta potential measurements will be replicated in the future to help justify the AgNP behavior during the column transport.

2.2.6. ION CHROMATOGRAPHY:

Working Principle

Ion chromatography is a class of liquid chromatography. A narrow tube is packed with ion exchange resin, serving as the stationary phase, and the mobile phase is forced continuously through the packed tube under pressure at constant flow rate. A sample is continuously up-taken at constant velocity or pressure in addition to the eluent and gradually separated into its ionic components. After being injection, a component is characterized by its retention time, which is the duration it requires to travel through the mobile phase, exit the column, and then reach the detector. Retention time is lower for solute molecules attracted to the mobile phase and higher for ones attracted to the stationary resin. Different ions are

separated into bands, which elute at different rates, reaching the conductivity detector at different times. The series of elution then translate into well-resolved chromatographic peaks, each with retention time characteristic of the ion's identity, and an intensity characteristic of the ion's concentration [91b, 85].

Sample Preparation

Chloride samples were stored at 4 ºC for no longer than 28 days until filtration and measurement [91a]. The eluent solution was prepared from stock solutions of sodium carbonate and sodium bicarbonate (Sigma Aldrich) diluted to 1.8 mM and 1.7 mM, respectively. A 0.5 mL aliquot of each sample and standard (prepared in 1% eluent) was filtered with a 0.45 µm filter, added into a polyethylene vial, and positioned at the automatic sampler rack. [91b]

Operating Conditions

In this study, ion chromatography was used to determine the concentration of the chloride samples and thus, to establish the breakthrough curve for the tracer. The ion chromatograph (Dionex ICS-1500) was equipped with an autosampler (AS400), an injection needle, a constant-volume loop, a guard column (Dionex), an analytical column (packed with an anion exchanger resin), a conductivity suppressor, and a conductivity detector. Samples were measured using a flow rate of 2 mL min^{-1}.

SPECIFIC AIM 2

2.3. FATE AND TRANSPORT OF SILVER NANOPARTICLES IN SATURATED POROUS MEDIA

2.3.1. TRANSPORT BACKGROUND INFORMATION:

One Dimensional Transport Setup

The experimental setup of the 1-D transport system in this study resembles that of the liquid chromatography column such that the continuously injected mobile phase comes in physical contact with the stationary phases at controlled pressure, allowing for certain equilibria in solute transfer [92]. Chloride ion (Cl^-) was selected as a reference due to its natural abundance in groundwater [54], waste water, and aquifers or aquitards, among other common minerals or inorganic ions [54]. Cl^- has been intensively used in studies of the transport of organic compounds, such as benzene rings and halocarbons [54, 92]. It was selected in this study as the solute-free, conservative tracer because its transport is governed strictly by advection and dispersion [54, 64]. This renders it distinguishable from the targeted contaminant, which may be affected by additional processes, such as nonlinear sorption, spreading, or the effect of hydraulic conductivity [92]. Upward injection of influent along with a valve-controlled bypass helps to prevent gas buildup and pumping delay of the influent's entrance into the column. The observed delay between the point of solute injection and the start of its elution at the outlet is a good indicator of the extent of the surface charge interactions of the media with the AgNPs as compared to Cl^- as tracer.

Breakthrough of an analyte may be interpreted by comparison to liquid (LC) or ion chromatography (IC), though IC only assumes reversible or equilibrium sorption. LC and IC similarly allow to retain various species at various rates depending on the media and solvent used in the column. A larger flow rate or particles with smaller size or low molecular weight generally allow for less mass capture and faster breakthrough. When the breakthrough of the solute is achieved, the adsorption is resumed and the desorption phase is started. Breakthrough is expressed as a frontal chromatogram that shows the evolution of an analyte at a fixed time or location in the filter bed as a function of adsorption parameters [54, 62, 93]. In this context, porosity is the ratio of void to total bulk volume [62].

Breakthrough Parameters

In this study, the breakthrough curve (BTC) indicates the evolution of the transported solute in the effluent, as the concentration of tracer or AgNP, as a function of time for a pulse influent. In this study, BTC was reported in dimensionless parameters in order to allow general extrapolation. Effluent concentration (C) was normalized through division by influent concentration (C_0) of AgNP [54]. Time was similarly normalized into a unitless pore volume quantity [54]. Pore volume is the volume available for the fluid phase to occupy at one point of time within a water saturated, porous media bed [54]. It represents a cumulative time scale, which is normalized using the volume of the aqueous phase present, and then voided of the excess volume held within the tubing and considered as injection delay. One pore

volume unit is the duration for pumping a volume of water into the column equivalent to the liquid volume within the media pore, at a constant flow rate.

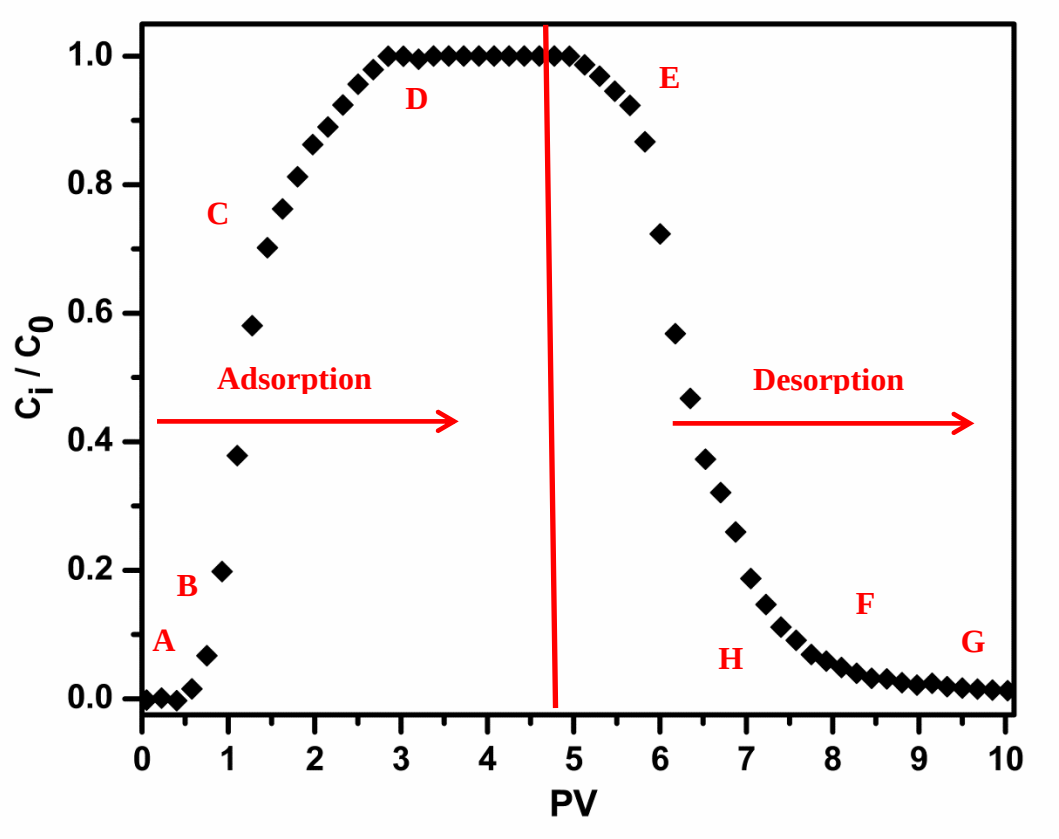

Figure 4: Simulated dimensionless 1-D breakthrough curve profile for a solute transported in a porous media bed, showing the phases of adsorption (breakthrough), desorption (elution) [94], and saturation (when $C = C_0$) for this study.

Figure 4 describes the typical adsorption and desorption, *i.e.*, breakthrough curve profile which indicates the different phases of transport. The effluent exits the column but is first void of any solute, while the influent is continuously pumped. Then, the influent front comes in contact with the first few layers of media, while part of it moves on and part of it is adsorbed onto subsequent layers of the media (phase A). The

adsorption continues, but not an appreciable amount of solute appears in the effluent, yet as solute is pumped continuously (phase B). The concentration of the solute increases gradually and more significantly in the effluent, and the bed of porous media becomes saturated with the solute (phase C) as the solute concentration in the effluent becomes very close to its initial concentration in the influent (phase D). The curve portion between B and D is known as the breakthrough of solute through the column. If this portion is extended, the adsorption is decreased due to the equilibrium established between the solute in the influent and in the bed. However, the solute injection is stopped and the solute-free, reference solution is now injected continuously to start the elution. A high concentration of solute still appears in the effluent (phase E); this is a slow start of desorption of the solute from the media. The concentration of the solute in the bed decreases until it reaches a minimum (phases F and G), where no more solute can desorb due to physical or chemical irreversible attachment to the media. The shape of the overall breakthrough curve, including slopes and symmetry, is determined by the flow rate, the concentration of influent, the sorption, and the adsorption equilibrium. [94]

The broader the plateau of the curve (D-E), the less significant is the advection force; whereas the narrower the curve is, the more significant is the dispersive force [54]. The area of the overall transport curve can provide information about the captured mass in the bed and the mass recovered in the effluent by difference with the solute concentration in the influent. Tailing (*i.e.*, decreased slope) and retardation [54, 94] (*i.e.*, shift towards the right) indicate reversible attachment of AgNPs to the media [65], related to rate-limited capture. On the other hand, a decrease in the breakthrough curve

area indicates irreversible capture or possible degradation and transformation [54, 94]. Tailing also indicates a rate-limited sorption [94, 110].

2.3.2. OPERATING CONDITIONS:

A one-dimensional (1-D) transport system (Figures 5–7) was assembled by mounting a cylindrical glass column (5 cm in length and 2.5 cm in inner diameter, borosilicate) vertically. The column was connected between a pump (0−100 R.P.M., MasterFlex, Cole-Parmer) at the inlet and a fraction collector (Spectra/Chrom CF-2) at the outlet through Teflon tubing (PTFE, 2 mm O.D., Cluxton). The column was packed with glass beads (45.00 ± 0.05 g of media) (Sigma Aldrich, 425−600 μm in diameter, acid-washed grade) and simultaneously bound by a fitting at each of the inlet and the outlet (Figure 5a). Each fitting consisted of a porous interface, which had been confined with 0.10 g of glass wool (Sigma Aldrich) (Figure 5b), and a valve control (vertical at the outlet and horizontal at the inlet) for flow control (Figure 5c). The column system was saturated with approximately six pore volumes (PVs) of 133 mg L^{-1} of the conservative tracer, namely potassium chloride (KCl). Breakthrough of AgNPs through the media bed was achieved after passing approximately 5.5 PVs (≈ 60 mL) of AgNP influent in the AgNP transport experiments and 4.5 PVs (≈ 50 mL) of tracer influent in the tracer transport experiments. One PV is approximately equivalent to 11 mL. Upon saturation of the media with the tracer, approximately 6 PVs (≈ 66 mL) of 15 mg L^{-1} of AgNPs (1−100 nm in diameter) were continuously injected into the column in upward direction for 60 minutes to investigate adsorption [54], at a flow rate of 1.0 mL min^{-1},

fixed ionic strength (0.01 mM of KCl), and pH (7.5). After each AgNP transport, the tracer was similarly injected for 60 minutes to investigate the desorption [54] of the AgNPs from the column. When the normalized concentration experimentally approached a certain maximum (at about 60 min), the background solution was passed again for desorption of AgNPs from the media surface. The effluent was collected as 2-mL samples at two-minute intervals in 14 mL vials (sterile, polystyrene, round bottom tubes, Fisher Scientific) through the fraction collector, which was programmed accordingly. The total collected effluent for both the adsorption and desorption phases was 120 mL for a total of 120 minutes at 1 mL min^{-1} flow rate. The column packed with porous saturated media contained about 42 mL of dissolved background salt solution. At the inlet, the flow rate of the pump was programmed at 1 mL min^{-1}. At the outlet, the collector was prompted to consecutively collect effluent at the end of every two-minute interval accordingly. The start of injection is considered to be Time Zero (t=0). At the beginning of this phase, the front-face AgNPs interact with the glass beads and emerge to the top (*i.e.*, the other end of the column). This is considered the delay between the injection and collection of the AgNP colloid.

2.3.3. SIZE-SELECTED AGNPS AND FLOW RATE TRANSPORT

Similarly, in some experiments, the influent was varied at the same conditions, and size-selected AgNPs, namely the 50 nm retentate (*i.e.*, the 50 cc, 50-100 nm in diameter) and the 100 kD retentate (*i.e.*, the 100 cc, 1−20 nm in diameter), were passed for 60 minutes through the column at 1.0 mL min^{-1} for adsorption.

Desorption was similarly performed for 60 minutes by passing the tracer at 1 mL min^{-1}.

Another set of experiments was performed, where the original colloidal AgNPs were similarly passed for overall sorption at the same conditions with the exception of the flow rate, which was varied to 2 mL min^{-1}. In contrast to the slower flow rate, the total collected effluent for adsorption and desorption phases from this set of experiments equaled 240 mL for a complete transport. It must be noted that the flow rate experiments were performed for the original Creighton AgNP colloid and will be repeated in the future for reproducibility. Flow rate experiments would require a more thorough future examination using absorption or emission spectroscopy for accurate quantification.

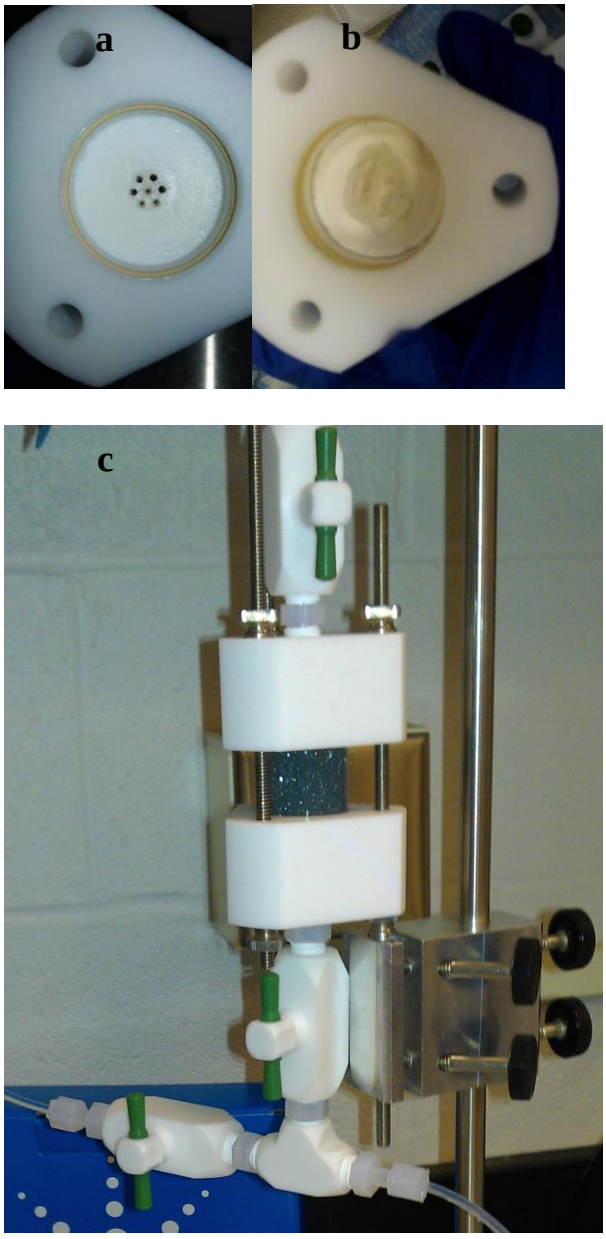

Figure 5: Photographs of the column fitting (a and b) which is placed at the inlet and outlet of the laboratory glass column to serve as a solid-liquid porous interface; the interface which is sealed with silk cloth (b) in order to prevent the porous media from exiting the column with the effluent; and the laboratory glass column (c) which is vertically mounted and connected to the bypass valves at its top and bottom.

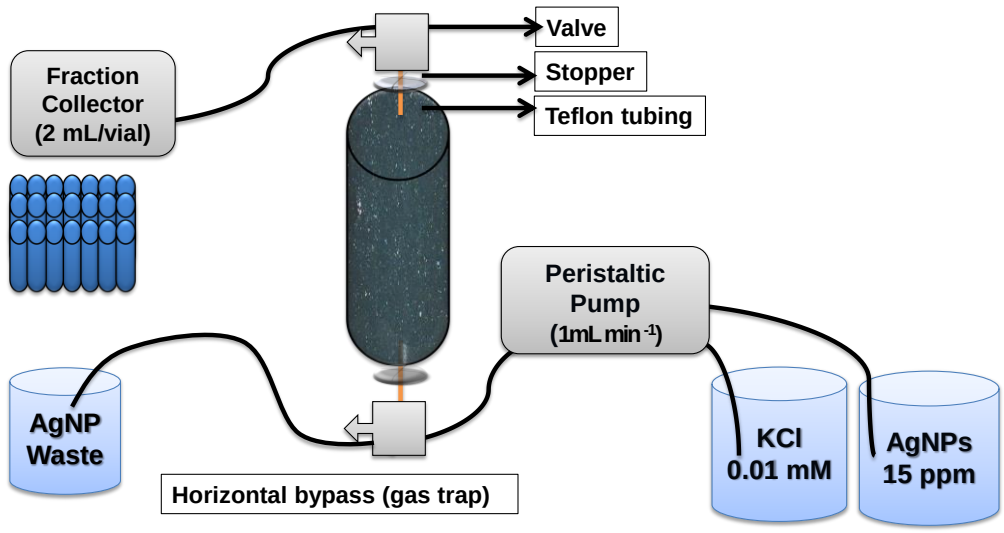

Figure 6: Schematic diagram of the one-dimensional transport system.

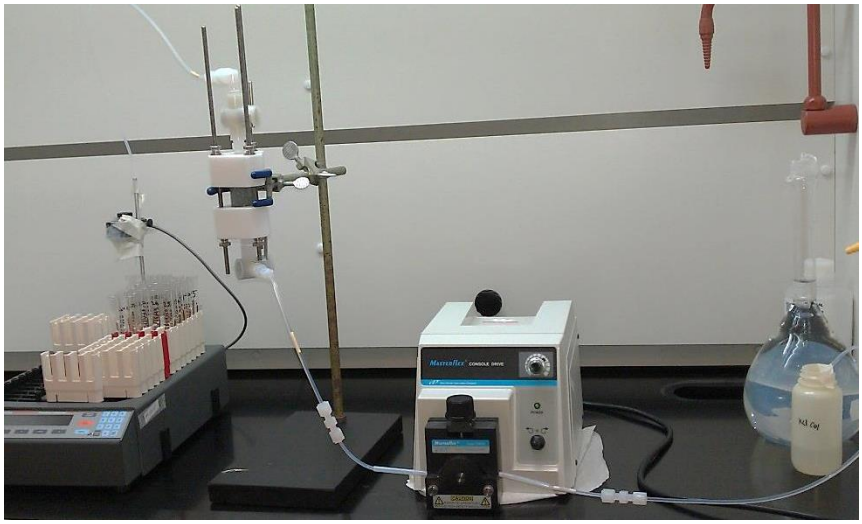

Figure 7: Photograph of experimental setup showing injection of tracer or silver nanoparticles (AgNPs) through the glass-bead packed column, as a bench scale simulation of AgNPs transport through subsurface water.

SPECIFIC AIM 3

2.4. EDUCATIONAL INSTRUMENTATION EXPERIMENTS:

The experiment entitled, *The determination of silver nanoparticle (AgNP) concentration by inductively coupled plasma optical emission spectrometry (ICP-OES)*, was incorporated into the Instrumental Analysis laboratory course (CHM 4350L) offered in Spring Quarter 2012 at WSU. I served as the graduate teaching assistant for this ICP-OES experiment in CHM 4350L and contributed to the development and successful implementation of the experiment together with my research colleagues. Atomic spectrometry is an analytical technique commonly used for the quantification of trace elements, such as alkali, alkaline, and heavy metals due to the absorption or emission of electromagnetic radiation by atoms or ions in a liquid [95, 96, 97]. In this educational experiment, ICP-OES was employed for the accurate quantification of the nanosilver amount in the Creighton colloidal samples of AgNPs.

2.5. ICP-OES WORKING PRINCIPLE

The *Varian Inc.* 710 ICP-OES instrument used in this experiment is equipped with: a) an argon gas source of a rate-controlled argon gas feed, b) a three-channel automated sampler (Autosampler, Sample Preparation System 3, Varian), c) a concentric nebulizer that depends on the Venturi effect, where gas flows through the two outer tubes that stream liquid through the innermost tube, a cyclonic spray chamber, d) a torch that is made of three concentric quartz tubes and is configured in the axial mode, e) a shutter to help recalibrate the measurements in between samples, f) a computer-optimized Echelle optical system for wavelength separation that is

designed with fixed optical parts to ensure the lowest detection limits and maximum stability, g) a 400 mm focal length polychromator that is temperature controlled to 35°C for high stability, h) a charge coupled device (CCD) array detector that has over 1.1 million pixels that can capture the entire spectral range in one reading, and i) a photomultiplier tube that decodes signal from the spectral line readings sequentially [85, 98]. A water-cooled induction (Tesla) coil, made of copper tubing that spirally surrounds the plasma torch, is powered by a radio-frequency (RF) generator. The liquid at the autosampler is constantly introduced via the peristaltic pump into the nebulizer and aspirated into the spray chamber, becoming an aerosol. The peristaltic pump also controls the nebulizer flow and empties excess liquid from the spray chamber through a drain vessel at a 200 psi pressure gradient [85, 99].

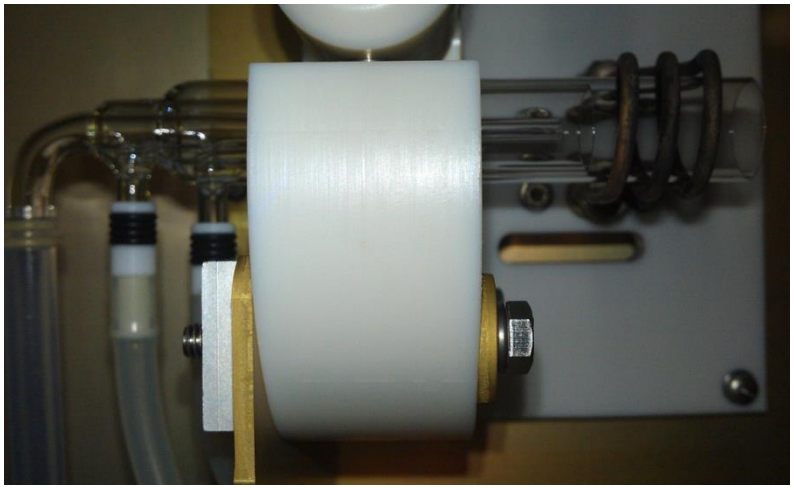

Figure 8: Photo of the ICP-OES torch that is surrounded by the copper coils and that contains the ignited plasma, which extends to the right side (710 Varian/Agilent – Instrumental Analysis Lab).

Figure 9: Photo of the ICP-OES nebulizer taken while the plasma was on. It illustrates its location at the right side of the spray chamber with respect to the operator (710 Varian/Agilent – Instrumental Analysis Lab).

The amount of the sample aspirated into the spray chamber depends on the time operating conditions. The gas carrier: a) creates a negative pressure through the nebulizer and spray chamber that causes a corresponding amount of sample to be aspirated into the spray chamber, b) generates an auxiliary flow between the intermediate tube and the injector tube in the torch, with a flow rate sufficient to extend the plasma away from the mouth of the torch, c) acts as the plasma source while purging the system, and d) helps to excite the analyte atoms by collisional transitions [85, 95]. An electromagnetic current is induced by the RF generator (at ~40 MHz) through the coil, creating a localized, homogeneous electromagnetic field along the torch at time-varying magnetic fields. The plasma is ignited once the gas is ionized by the spark from the coil. It is then maintained through their continuous interaction.

The plasma appears as a light blue cone within the torch and has a thin, sharp tail that extends away from the torch. Electrons are generated by the magnetic field upon excitation of the analyte atoms. At high speeds, the Eddy current, that is abundant in cations and electrons due to excitation and relaxation transitions, collides with the gas raising the temperature [100]. The plasma functional regions are divided into: the preheating zone where vaporization atomization of analyte occurs (to decompose it into atomic vapor), the initial radiation and normal analytical zone where ionization and excitation of the gas atoms occur followed by emission, the induction region where the analyte atoms receive the highest energy with a high background, and the tail plume which is relatively cool [95]. In the plasma, the rate constant of dissociation is at least 2000 times the rate constant of ionization [101]. A mini peristaltic pump on the automated sampler controls the flow rate of the rinsing solution in between sample measurements. Positioned axially (parallel) or radially (perpendicular) with respect to the plasma, the torch harbors the inert cooling effect and the contact between the sample analyte atoms with excited argon molecules [85, 95]. Some ICP-OES instruments have the option to switch the viewing arrangements; however, the axial position provides increased radiation intensity and precision by granting the longer path length [85, 95].

The Creighton colloid may contain by-products and/or excess reagents that can cause matrix interferences in ICP. The U.S. EPA classifies matrix interferences as physical (*i.e.*, surface tension that affects nebulization), chemical (*i.e.*, solute vaporization or refractory reactions in the matrix that are unmatched by quality control), or otherwise spectral (*i.e.*, unresolved overlap, background emission due to

recombination phenomena, and stray light due to emission of highly concentrated elements) [102a]. The plasma is advantageous for atomic absorption over other excitation sources due to its capability for multielemental analysis, low detection levels at the low part per billion (ppb or μg L^{-1}) levels, matrix effect minimization [85], and a linear dynamic range that can extend a 100 fold [95]. Its power is attributed to extremely high temperatures (6,000–10,000 °K) that are 10-fold higher than the flame or furnace temperatures (2000–4000 °K) [95] and to the inert atmosphere that allows many energy level emissions to be populated simultaneously and detected [85]. ICP-OES is especially effective for speciation of transition metals due to the high degree of excitation [103]. The high nebulization pressure (200 psi) allows efficient aerosolization of the sample molecules, while the extreme plasma temperature causes faster vaporization [96] of the aerosol. Furthermore, this is not applicable for elements common in the air or nonmetals, such as H, He, C, N, O, F, Cl and Ne [104]. Due to the constant cooling and uptake requirements, torch damage (devitrification, crystal growth of salts and organic material) must be avoided. The maintenance of ICP-OES parts may not be cost-effective [103]. Therefore, extensive glassware cleaning and thorough sample preparation are both recommended [102a] in order to avoid clogging and potential damage to the nebulizer and the torch [102a].

2.6. SAMPLE AND STANDARD PREPARATION FOR ICP-OES MEASUREMENTS

Corresponding aliquots of the influent (original AgNP colloid, the 50-nm filtrate, the 50-nm concentrate, and the 100-kD retentate) or the effluent samples of AgNPs were added to 2 mL of the nitric acid (65–70% assay, OPTIMA Grade, Fisher Scientific) into class A, 40-mL digestion beakers (Fisher Scientific) and allowed to digest at room temperature for 15 minutes (cold digestion) [105]. Next, the samples underwent hot digestion on a preheated hotplate for two hours at 225 °C. Upon complete evaporation, the samples were removed from the hotplate surface and quantitatively diluted in class A Volumetric flasks (Fisher Scientific), in a matrix of 2% V/V nitric acid and ultra-purified water (18 MΩ·cm). To avoid memory or carry-over interferences, the expected, final concentrations were bracketed by the analytical calibration range, while satisfying the linearity conditions [102]. A set of 10 standards (of 0.003, 0.010, 0.025, 0.050, 0.100, 0.250, 0.500, 1.00, 2.50, and 5.00 μg mL^{-1} of Ag) was prepared from an ionic silver nitrate stock solution (1000 μg mL^{-1} of Ag, Certiprep Spex, ICP-MS grade) in a sample-matching matrix. After digestion and 100-fold dilution of the AgNP colloid, a set of standard-additions were prepared for elimination of possible matrix effects that may not be indicated through the external calibration curves. The ultrafiltration samples were diluted accordingly to match the calibration range at 1000 to 10,000 fold. Equal volumes (5 mL) of the diluted samples were collected and spiked with increasing volumes (0, 25, 50, 75, and 100 μL) of the 10 μg mL^{-1} Ag^{+} standard. To prevent spectral interferences due to the presence of Na or possible deviation in the instrument's optical components, two wavelengths of Ag were included.

2.7. ICP-OES ACQUISITION PARAMETERS

The following acquisition parameters were applied: wavelength for Ag (328.068 nm), radio frequency (RF) power (1.20 kW), plasma flow (15.0 L min^{-1}), auxiliary flow (1.50 L min^{-1}), and nebulizer pressure (200 kPa). Each solution (blank, standard, and sample) was measured in triplicates using a replicate time of 10 s, a between-measurement stabilization time of 15 s, a sample uptake delay of 40 s, and a rinse time of 15 s. All data was exported as a *Comma Separated Value* file for data analysis. The direct instrument response (emission intensity) was plotted against analyte molecule concentration or standard addition aliquot volume for the external calibration and the standard addition method, respectively. Linear interpolation of silver concentration in the AgNP samples was performed by regression analysis and with account for the dilution. *Microsoft Excel* and *OriginPro 8.5* software programs were used for data analysis and graph construction.

3. RESULTS AND DISCUSSION

SPECIFIC AIM 1

3.1. SHAPE, SIZE, CHEMICAL COMPOSITION, AND SOLUBILITY

Noble metal NMs have the capacity: 1) to collectively polarize their surface electron density by aligning the free s-orbital electrons of the outermost shell along the incident electrical and/or magnetic fields transversely or longitudinally, and 2) to yield absorption at corresponding incident frequencies [13]. This effect, known as the surface plasmon resonance (SPR), is optimal for specific NM shapes, orientations,

and sizes much smaller than the incident wavelength, giving rise to an exponential amplification of absorption, Rayleigh scattering, and fluorescence (inelastic) or transmitted Raman (elastic) signals. As NM size decreases, electrons undergo larger quantum confinement and the band gap energy increases, yielding semi conductive properties for so called quantum dots that have radii of Bohr size or smaller [13].

AgNPs will absorb light in the purple spectral region and will transmit light in the yellow to brown region [13, 86]. The sharp, symmetrical profile of the SPR peak, which was observed at 400 nm (Figure 10) in the UV-Vis absorption spectrum, is indicative of AgNPs of a spherical geometry and a moderate size distribution (mainly within the 1–100 nm range).

For a fresh AgNP colloid, the SPR peak at λ_{max}, 400 nm, was characterized by an approximate maximum absorbance of 1.70 a.u. (Figure 10). The Lambert-Beer law in conjunction with this absorbance value allowed to roughly estimate the nanosilver concentration as being 0.099 mol L^{-1} or 10.7 mg L^{-1}. SPR peaks of influent and effluent AgNP ranged between 390 and 410 nm. Peak intensity declined at lower concentrations and shifted toward smaller wavelengths for effluent AgNP samples.

The following parameters were also utilized in this concentration calculation: the extinction coefficient reported by Ershov and Gordeev for spherical AgNP clusters of 10–20 nm diameter [86] ($\varepsilon_{400\ \mathrm{nm}}$ of 1.9×10^4 dm^3 mol^{-1} cm^{-1} or 19,000 L mol^{-1} cm^{-1}), the path length of the cuvette (1 cm), and the molar mass conversion for atomic silver (1 mol that is equivalent to 107.8682 mg). This agrees with the previously estimated 11 ppm [76]. A more accurate quantification of the

nanosilver concentration in each colloidal sample was achieved through ICP-OES measurements.

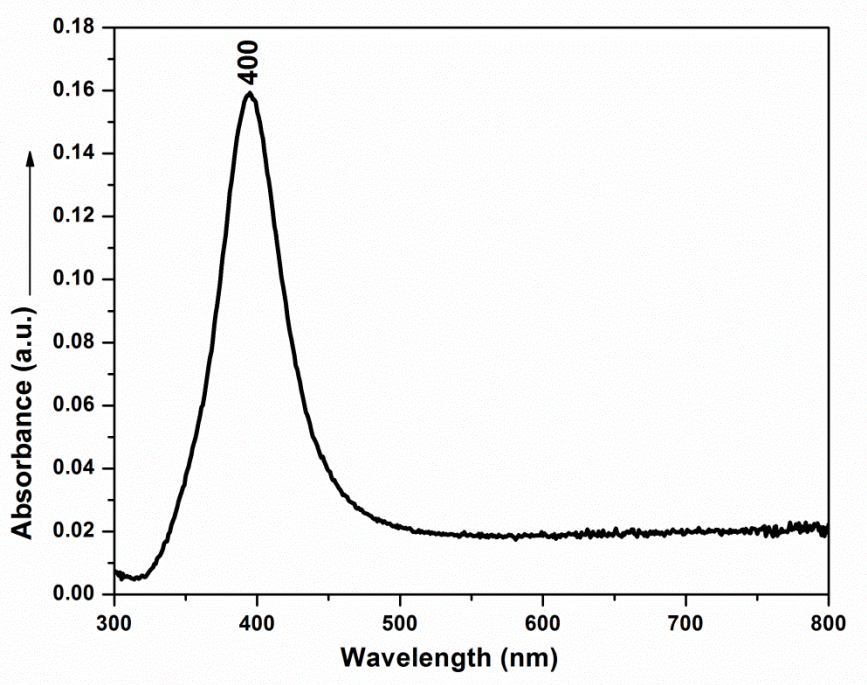

Figure 10: Ultraviolet-visible absorption spectrum of a fresh Creighton colloid of AgNPs recorded at ambient temperature.

Raman spectroscopy verified the purity of the colloidal samples and their suspension in water [76]. The Raman spectrum (Figure 11) of a fresh Creighton colloid of AgNPs exhibited solely the vibrational fingerprint of water, which has two main features: a single peak at 1640 cm^{-1} and a doublet peak at 3240 and 3420 cm^{-1} representing the bending and stretching vibrational modes of O-H respectively [76]. The lack of strong features between 100 to 600 cm^{-1} indicates absence of B-H, C-H [87], Ag-S, AgO or Ag_2O, AgCl, C-O-Ag, and Ag-C [107]. The lack of noise between

500 and 2000 cm^{-1} indicates absence of N-O and of other groups related to organic impurities [87, 107].

The original Creighton colloid of AgNPs was found to be stable for several months upon refrigeration storage. Storage at room temperature or higher temperatures may cause the hydrolysis of sodium borohydride [75, 76]. Literature suggests that the stability of the colloid is due to a negative layer of ions (*e.g.*, borate and nitrate [75], or citrate [51]) surrounding the zerovalent AgNP surfaces in the aqueous suspension. No evidence of AgNP degradation or impurification was found following the transport. The variation in Raman band features did not exceed 1%, *e.g.*, the percent difference in the water bending band was found to be 0.61% between the influent and effluent nanosilver. Although no oxidation was evident through Raman spectroscopy, oxidation of effluent AgNP may have occurred to some extent. Oxidation and reduction was reported to cause changes in the SPR absorption profile [86], which were not observed in this experiment. In this study, the original Creighton colloid was utilized in transport experiments one or two days following preparation.

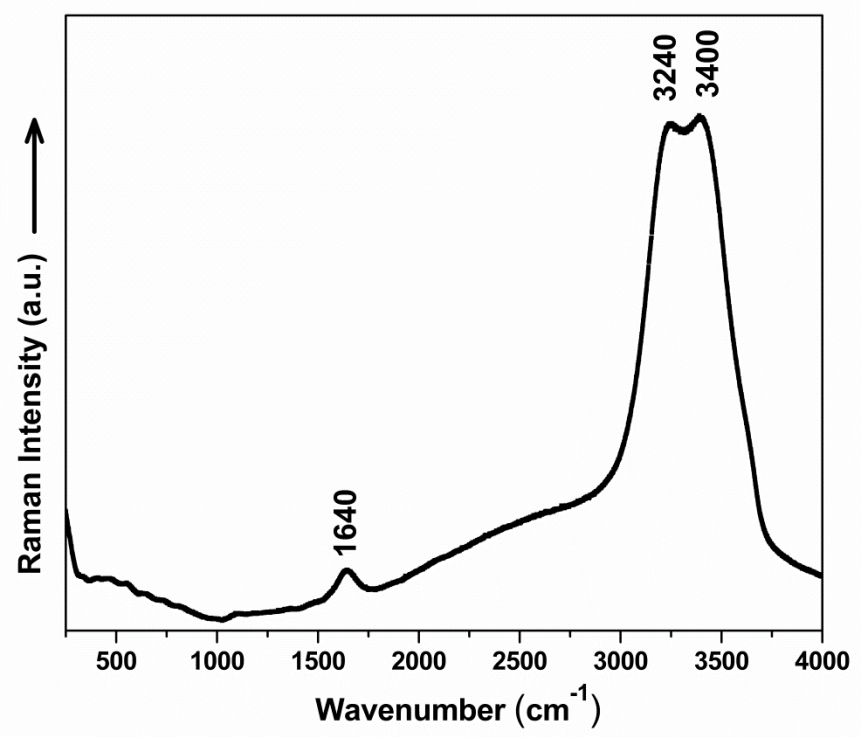

Figure 11: Raman spectrum of a Creighton colloid of AgNPs, representative of the influent and effluent AgNP samples.

The TEM measurements validated the size of the AgNPs. The abundance and area data of AgNPs was exported from *Image J* into *Microsoft Excel* for diameter calculation and then into *OriginPro 8.5* to construct a discrete distribution histogram of the cumulative frequency as a function of the AgNP size. Previous TEM studies reported that these Creighton AgNPs commonly have an average diameter of about 11 nm [75] and that they typically fall within 1– 10 nm or 1–50 nm in overall diameter range [74]. TEM measurements in this study have confirmed the reported average diameter (11 nm, Table 2), round shape and moderate size distribution of the Creighton colloidal AgNPs (1–180 nm, Figures 12 and 13). They also manifested the

efficacy of tangential flow filtration (TFF) in size selecting the original colloid and producing the two, 50 cc and 100 cc, retentates (Figure 10). Both contained aggregates shown as darker outlines in the TEM images (Figures 12 and 13c).

The occurrence of aggregates in the collected retentate sample cannot be prevented especially in the absence of surfactants. It should be particularly noted that a small number of irregular aggregates of triangular form or pentagonal shape were observed in few TEM images of the 100 cc retentate (Figure 13a, 13b) perhaps due to the ultrafiltration process and TEM drying effects. Compared to dead-end filtration, where pores are more readily obstructed by the trapped particles [81], recirculation filtration allows more efficient concentration and purification but may cause formation of larger AgNPs upon collisions of particles with the filter membrane [81]. Filter cleaning and conditioning is key for eliminating aggregation and deformations and ensuring homogeneity. Previous concentration recoveries using the TFF system on Creighton AgNPs were reported to be as high as 70%–90% [109]. Aggregation of suspended AgNPs and subsequent formation of other AgNP shapes were previously attributed to organic contaminants, and steric or electrostatic repulsion [67].

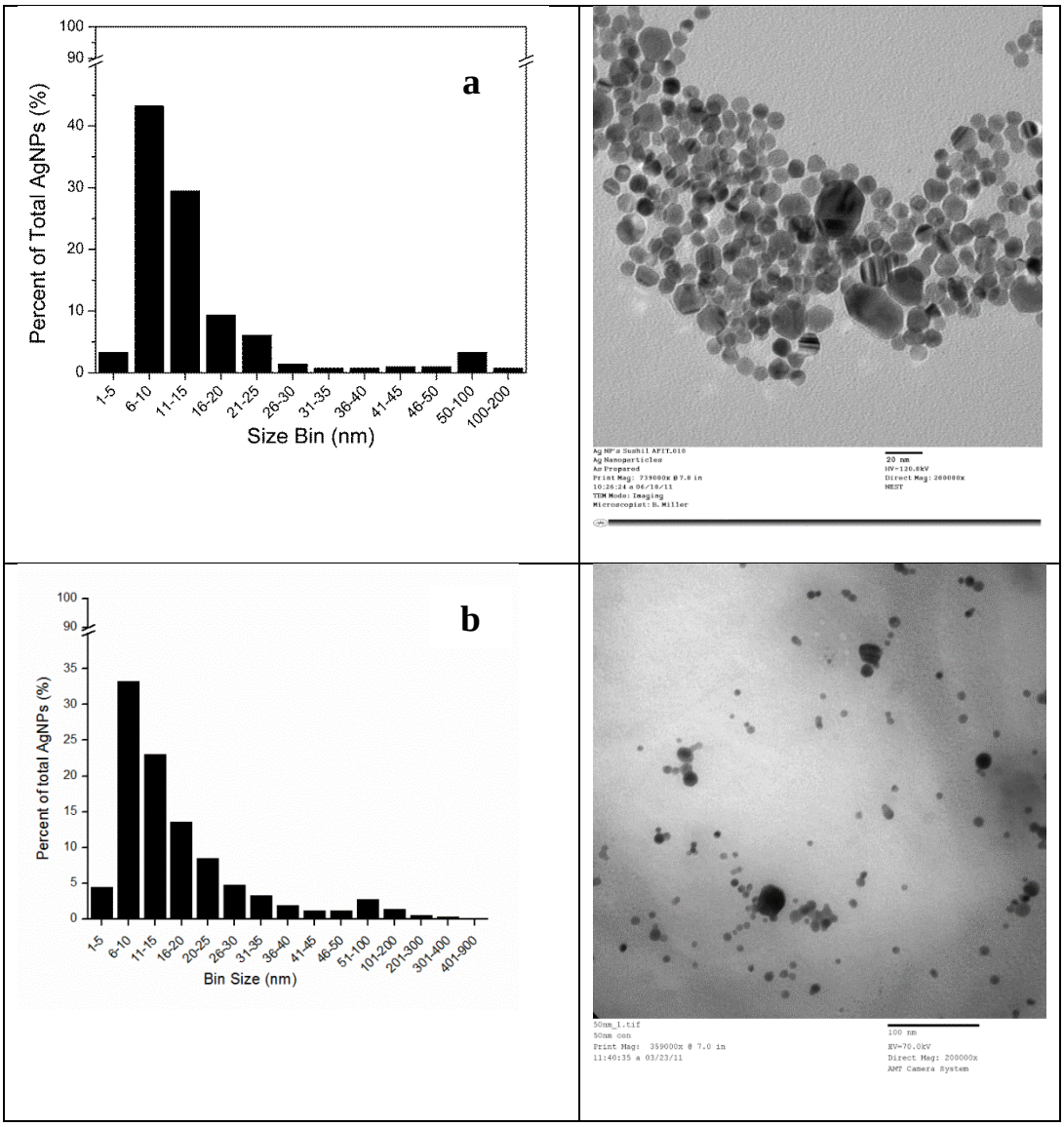
a
Percent of Total AgNPs (%)
100
90
40
30
20
10
0
1-5
6-10
11-15
16-20
21-25
26-30
31-35
36-40
41-45
46-50
50-100
100-200
Size Bin (nm)
b
Percent of total AgNPs (%)
35
25
15
5
1-5
6-10
11-15
16-20
20-25
26-30
31-35
36-40
41-45
46-50
51-100
101-200
201-300
301-400
401-900
Bin Size (nm)

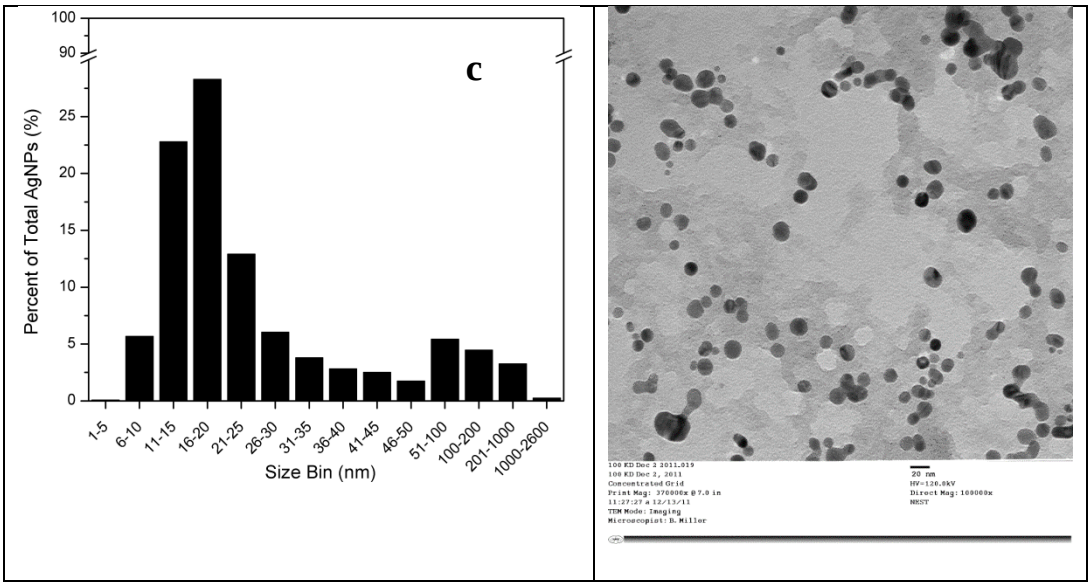

Figure 12: **Left**: TEM size histograms (N = 400) illustrating the AgNP size distribution of the original Creighton colloid (a), the 50 nm retentate (*i.e.*, 50 cc) (b), and the 100 kD retentate (*i.e.*, 100 cc) (c) at scale bars of 20, 100, and 20 nm respectively. **Right**: TEM representative images of the corresponding AgNP samples.

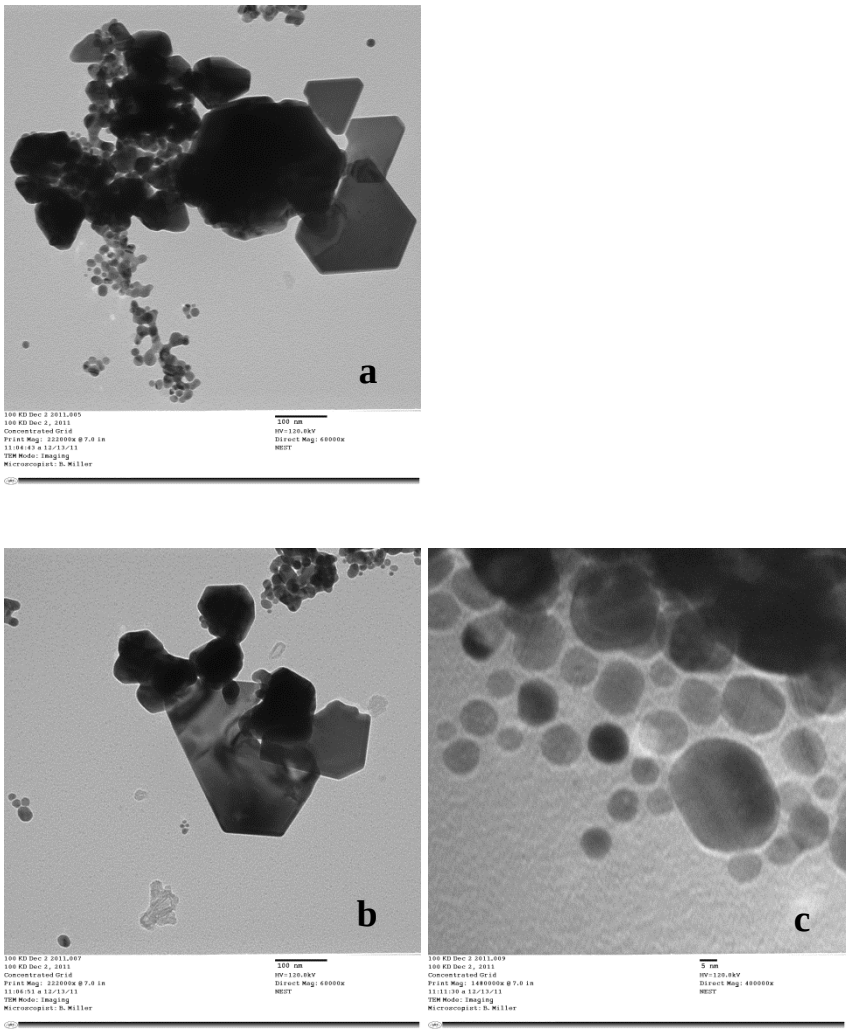

Figure 13: TEM images of atypical AgNPs that were observed in the 100 kD retentate (100 cc) at resolution of 100 nm (a), 100 nm (b), and 5 nm (c).

The amount of total silver in the colloidal samples was interpolated using regression analysis of the corresponding external calibration curve (Equation 3).

$$\mathbf{y = mx + b} \qquad \textbf{Equation 3}$$

In Equation 3, x represents the concentration of the silver in the digested sample or standard, y represents the corresponding instrument response (the emission intensity

characteristic of 328.068 nm), *m* is the slope or dy/dx (rise to fall ratio, which describes the linearity of the calibration fit), and *b* is the y-intercept.

In FAAS, one calibration curve was used (Figure 14), while in ICP-OES, the calibration was divided into two analyses in order to ensure dynamic linearity. Equation 4 describes the calculation of the total silver concentration in the digested liquid samples using results from FAAS and ICP-OES measurements.

$$\mathbf{C = \frac{A \times B}{V}} \qquad \textbf{Equation 4}$$

In Equation 4, *C* is the final concentration of nanosilver in the analyzed sample, *A* is the interpolated concentration of metal in the digested sample solution (mg L^{-1}) obtained from the external calibration by using the linear fit Equation 3, *B* the final volume of digested solution (mL), and *V* is the sample size (mL) [108].

The average value for the triplicate ICP-OES measurements was 15.20 µg mL^{-1} of Ag (Table 2). This agrees well with the previously reported theoretical yield of 15.42 µg mL^{-1} for the Creighton colloid [75]. While the overall ICP-OES calibration analyzed using all the prepared standards (3 to 2000 µg L^{-1}) yielded good linearity (approximately r^2 of 0.9996 to 0.9998), elimination of outliers was required and the dynamic range was limited compared to the expected concentrations of silver. Therefore, ICP-OES calibration linearity was enhanced by employing two distinct calibration curves that bracket the lower and upper expected concentrations separately (Figures 15 and 16).

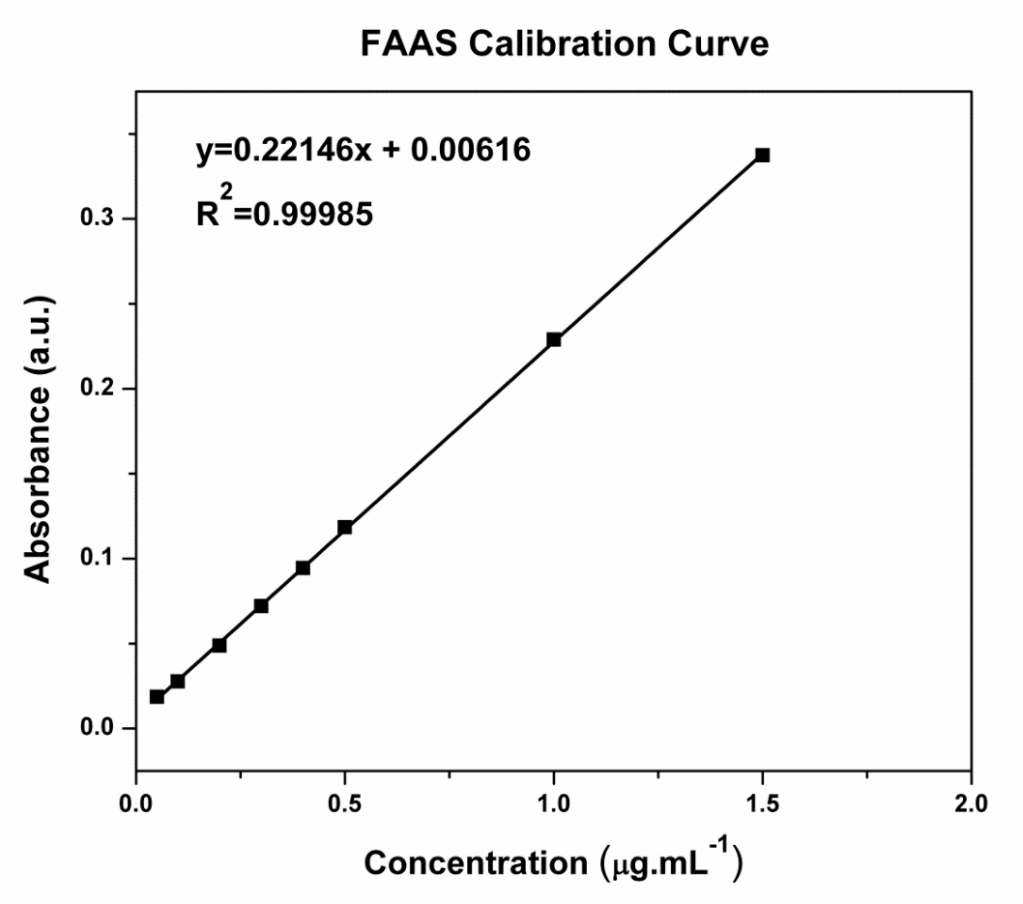

Figure 14: FAAS external calibration curve constructed using eight silver standards of 0.05, 0.1, 0.25, 0.3, 0.4, 0.5, 1.0, and 1.5 μg mL^{-1}.

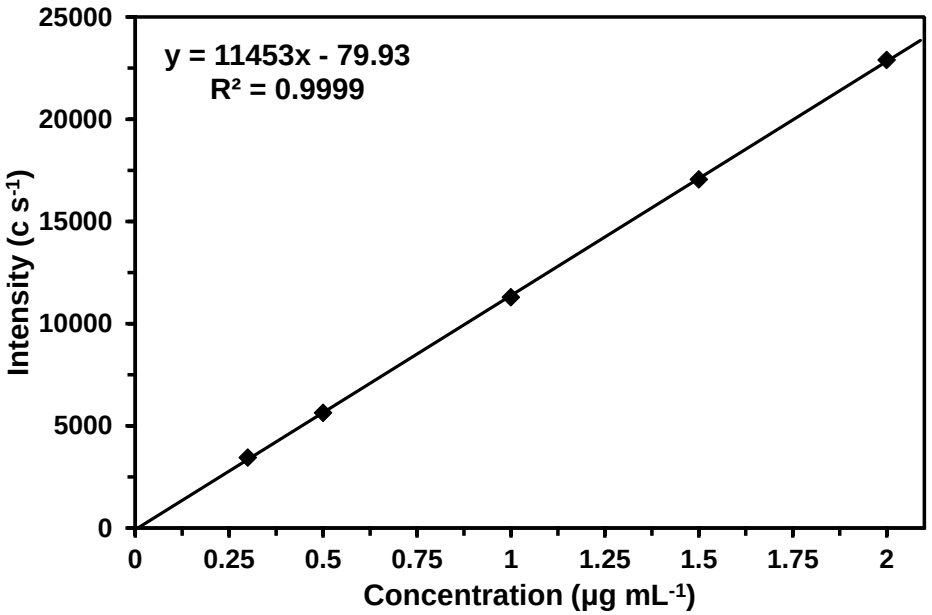

Figure 15: ICP-OES external calibration curve constructed using five silver standards of 300.0, 500.00, 1000.0, 1500.00, and 2000.0 µg L^{-1} to bracket the upper range concentrations.

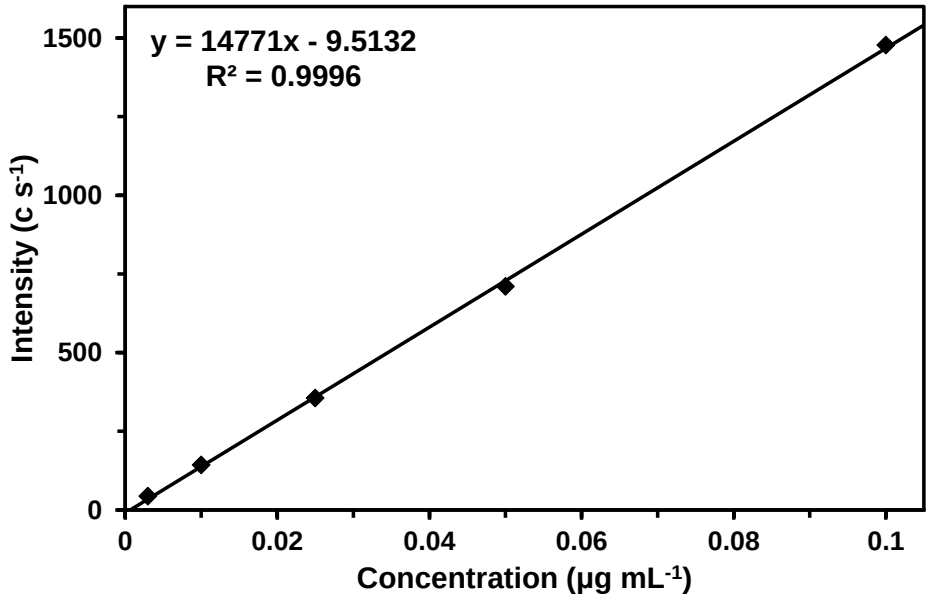

Figure 16: ICP-OES external calibration curve constructed using five silver standards of 3.0, 10.0, 25.0, 50.0, and 100.00 µg L^{-1} to bracket the lower range concentrations.

Table 2: Average size and concentration of AgNPs as determined by TEM and ICP-OES for the filtration products: the original Creighton colloid, the 50 nm retentate (50 cc), and the 100 kD retentate (100 cc). At least *N* = 400 AgNPs were analyzed in *Image J* software before determining the average size of AgNPs in each colloidal sample.

	Original colloid	50 nm concentrate	100 kD retentate
Nanosilver concentration (µg mL^{-1} or ppm)	15.20	900	8,550
Average size of AgNPs (nm)	9.30	22.23	11.10
Size range (nm)	1.0 – 180	20 – 180	1.0 – 80
Number of Analyzed Particles (N)	800	500	500

3.2. SURFACE CHARGE

Zeta potential measurements were performed for pH-modified and size-selected AgNPs (100 cc of 1-20 nm and 60-70 µg mL^{-1}) at ambient room temperature to investigate the AgNP surface charge. A "sol" is a suspension of NPs in a solvent, indicating a distinct form of 'solubility' that is maintained by balanced electrostatic interactions and zwitterion layers that affect its overall stability [75, 76]. Electrostatic

interactions are maintained by an electrical layering between the metal NPs and the surrounding anions in the sol, minimizing aggregation [75, 76, 77].

The impact of pH on the colloid stability has been noted in the literature [45, 109, 111, 112]. It was found that AgNPs dissolve at low pH and aggregate at high pH. Going from pH 6 to 2, Creighton AgNPs aggregate and the colloid tends to collapse [109, 112]. It was observed that the Zeta potential of the Creighton AgNP colloid changed from 6.5 mV at PH 2 to -56 mV at pH 11 with a point of zero charge at pH 2.7. The stability of pH-modified colloids was corroborated with surface charge with the colloid's SERS signal enhancement capability [109, 112].

AgNP surface charge was found to be negative throughout the pH range 3.5–10 and to increase in magnitude with increasing pH (Figure 17). The point of zero charge for AgNPs was attained around pH 3.1 for this study in good agreement with the literature [112]. The Creighton AgNPs had Zeta potentials ranging from -29 to -61 mV for pH of 3.9 and 10.3, respectively (Figure 17). The hydrodynamic size of the AgNPs in this study was found to be approximately 100 nm throughout the pH range 2–9 indicating no impact of pH on hydrodynamic size of AgNPs. This was not reported in the graphs along with the Zeta potential data because it could not be replicated for the 100 cc retentate prepared for the Zeta Potential measurements. Deviations in the samples' pH may have been caused by expected fluctuations in room temperature (25 ± 3 °C). One anomalous value was found at pH 6.6 and was deemed as an outlier, with two replicate measurements remaining.

Zeta potentials of large magnitudes (*i.e.*, 30 mV or above) are correlated with good dispersivity and stability, whereas potentials of low magnitude (*i.e.*, < 20 mV), which occur at acidic pH, usually indicate faster aggregation with exceptions [45]. Therefore, it is expected that the 100 cc retentate used for Zeta potential measurements has a desirable stability for colloidal applications [45]. The pristine Creighton AgNP colloid has a pH of 7.80; therefore, AgNPs may have a negative, large surface charge around neutral pH. Thus, the AgNP suspension is highly stable and fairly robust to withstand environmental changes at the tested conditions of this study. Moreover, experimental observations of the pH-modified 100 cc samples that were used for Zeta potential measurements showed a longer shelf life at pH of 7.5 and above compared to the samples with pH of 6 or lower. While the former preserved their color for at least 18 months, the latter aggregated in less than 6 months. The 50 nm retentate was found to have a slightly higher pH (8.4). The 100 cc retentate's pH of 7.5 corresponds to a Zeta potential of approximately -41 mV for the 100 cc in this study, which is a large magnitude, indicating good stability of the colloid.

In general, pH was shown to have a moderate effect on the surface charge of AgNPs in the 100 cc for this study. The surface charge of the AgNPs was negative at neutral pH, indicating that the surface charge plays an important role in the AgNP facilitated transport through the polar silica glass bead pores.

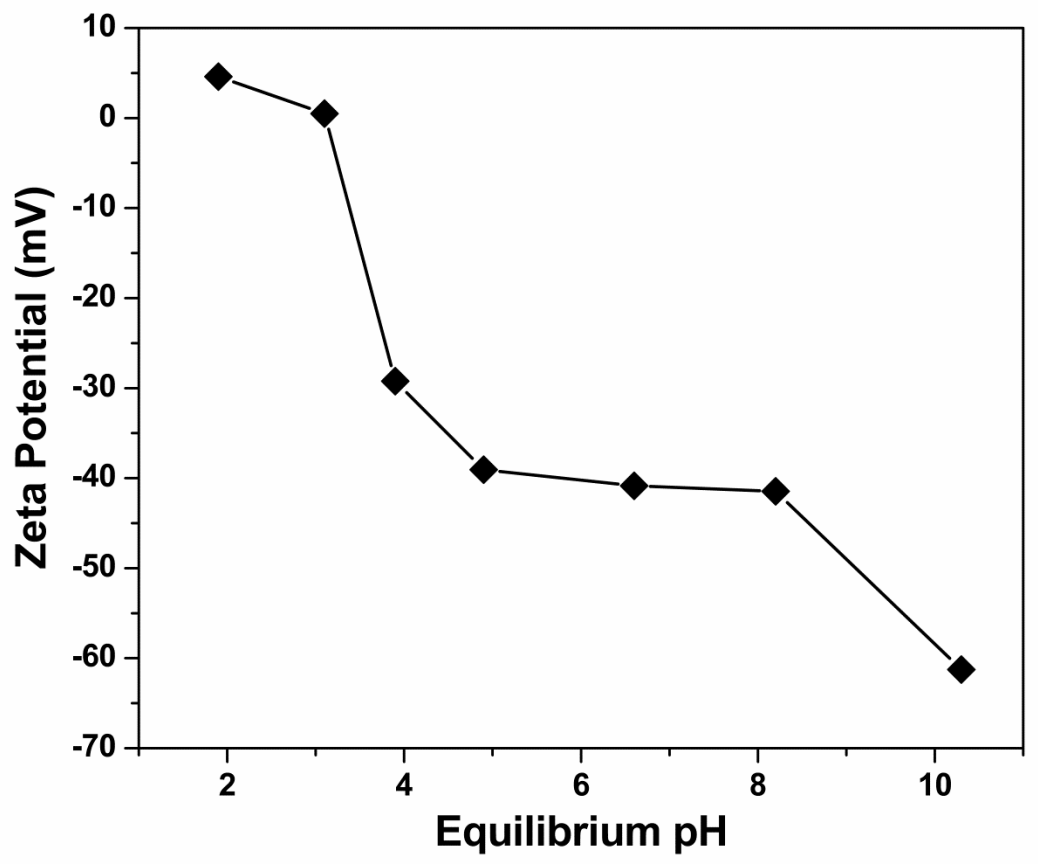

Figure 17: Zeta potential of the pH-modified batch AgNP, 100 kD retentate (100 cc) samples is reported as an average of triplicate measurements and plotted as a function of the 1.9–10.3 pH range.

In other studies, citrate-reduced AgNPs exhibited similar negative potentials with most effective electrostatic and steric stability (-27 to -33 mV (± 5 mV) for pH of 6–8 [109]. Borohydride-reduced AgNPs, that are comparable to the colloids in this study, exhibited a wider range (-5 to -45 mV) of Zeta potential that is in the window for SERS detection enhancement, compared to citrate-reduced silver or gold nanoparticles [112]. The potential of -40 mV correlated to a pH of 8.

El Badawy *et al* similarly reported potential for pristine $NaBH_4$-AgNPs with a TEM average diameter of 14 nm, to be -38 mV at pH 8.7, close to the potentials reported with ionic strength modification [68]. The same group similarly reported aggregation of AgNPs occurring at low pH and high ionic strength [69a]. On the other hand, commercially obtained AgNPs, with a TEM diameter average of 17 nm and hydrodynamic size of 30 nm, exhibited potential between -8 and-16 mV at pH range 3–11, with a notable decrease to -17 mV at pH range 3–7 and a recovery to -10 mV at pH range 7–9 [113]. This indicates the necessity to evaluate the stability of suspensions with various size and composition in order to establish a clear mechanism of the NP surface behavior.

SPECIFIC AIM 2

3.3. FATE AND TRANSPORT AND BREAKTHROUGH CURVES

The breakthrough curves were constructed using the AgNP concentration as estimated through UV-Vis absorption spectroscopy. The concentration of total silver was also determined through FAAS and ICP-OES using Equation 3 and Equation 4, respectively, in order to confirm the UV-Vis absorption results. These measurements accurately quantified the mass recovery of AgNPs in the effluent and the mass capture of AgNPs within the porous media (Table 3).

The transport-breakthrough was reported in dimensionless parameters (concentration ratio versus pore volume) in order to facilitate extrapolation and

compare with similar studies in the literature. Equation 5 illustrates the conversion of a dimensional time (t_i) into non-dimensional pore volumes, while Equation 6 is used to calculate the normalized, dimensionless concentration as a ratio.

$$PV = \frac{Q\,t_i}{V_{col}} = \frac{v\,t_i}{L} \qquad \textbf{Equation 5}$$

In Equation 5, *PV* represents the pore volume or dimensionless time in pore volumes, *Q* is the flux or the flow rate of influent through the column (mL min^{-1}), *v* is the average pore-water velocity (Length/Time), t_i is the cumulative time quantity that corresponds to the time the effluent sample was collected, *L* is the column length (Length). V_{column} represents the volume of liquid allowed within the column (mL) throughout the transport experiment. V_{system} may be subtracted from V_{column} in order to exclude the delay volume within tubing that is outside the column boundaries. In this study, the time interval used for the cumulative time scale was designated as two minutes for efficient analysis purposes.

$$C = \frac{C_i}{C_0} \qquad \textbf{Equation 6}$$

In Equation 6, C_i is the concentration of the effluent solution, and C_0 is the concentration (Moles/$Length^3$) of the influent solution [54, 110].

The breakthrough appeared to indicate that transport was consistent with a model that described the following processes: advection, dispersion, irreversible capture, and rate-limited attachment/detachment. If the mass of AgNPs in the effluent, as calculated from the breakthrough curve, is less than the mass in the influent, then mass capture (irreversible attachment) has occurred. In this study, mass

capture was computed in two ways: 1) determining the mass leaving the column in the effluent by applying the trapezoidal method to calculate the area under the breakthrough curve (Table 3), and 2) using acid extraction to experimentally measure the mass of AgNPs retained within the porous media (Table 4). Pulse injection is a finite injection within the domain.

$$\mathbf{m_i = C_0 \times V_0} \qquad \textbf{Equation 7}$$

$$\mathbf{m_e = \sum(C_i \times V_i)} \qquad \textbf{Equation 8}$$

$$\textbf{Percent of mass recovered} = \frac{m_e}{m_i} \times 100 \qquad \textbf{Equation 9}$$

$$\textbf{Percent of mass captured} = \frac{\mathbf{m_i - m_e}}{\mathbf{m_i}} \times 100 \qquad \textbf{Equation 10}$$

Equations 8 and 9 describe the arithmetic calculation of the recovered mass using the sum of the trapezoids contained under the breakthrough area. m_i is the influent mass (μg), m_e is the effluent mass (μg), C_0 is the concentration of injected AgNPs in μg mL^{-1}, V_0 is the mass of the volume of injected AgNPs (mL), C_i is the concentration of the effluent sample (μg mL^{-1}) collected at interval t_i, and V_i is the volume of each effluent sample (mL). Mass capture may be estimated by mass difference using Equation 10 with no account for mass loss that is excluded in the capture-recovery balance.

Retardation of the NPs in comparison with the chloride tracer indicated that the NP transport is affected by reversible capture. It is expected that the retardation of breakthrough would be more pronounced for larger NP sizes (Figures 20, 21) and

slower flow rates (Figure 19). That is because the smaller particles flowing at higher velocities would be less likely captured within the media. Any experimental delay of AgNP flow was prevented through the bypass between the pump and the column.

Figure 18: Image of the influent of colloidal AgNP compared to an effluent sample of AgNPs collected at a time that corresponds to the plateau in the breakthrough curve, upon transport through the 5-cm column.

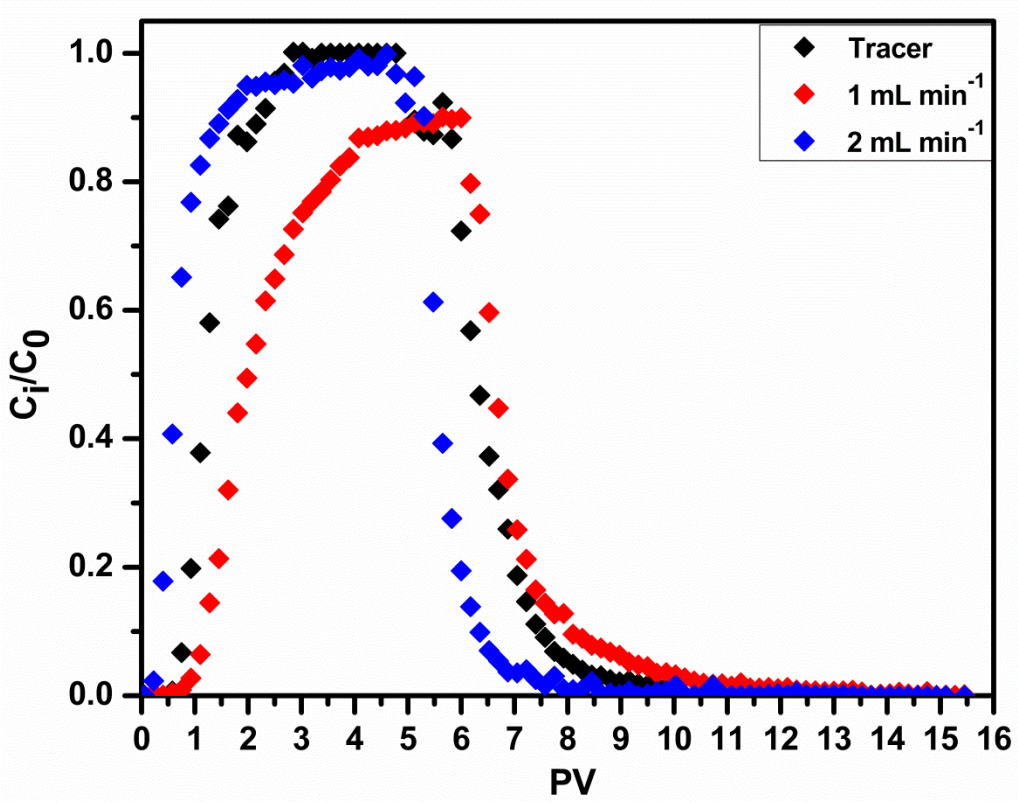

Figure 19: Non-dimensional breakthrough curve of Creighton AgNPs analyzed by UV-Vis absorption spectrophotometry and of Cl^- tracer analyzed by Ion Chromatography measurements. The plot was constructed in *OriginPro 8.5* software at: a depth of 5 cm, influent concentrations of AgNPs of 15.3 mg L^{-1} and KCl of 133 mg L^{-1}, flow rates of 1.0, and 2.0 mL min^{-1}, and fixed pH of 7.8.

Table 3: Mass capture analysis of the flow rate transport experiments.

Flow Rate	**1.0 mL min^{-1}**		**2.0 mL min^{-1}**	
	Mass Recovered	Mass Captured	Mass Recovered	Mass Captured
Retained mass		23.2%		9.18%
BTC Analysis	76.0%		88.9%	

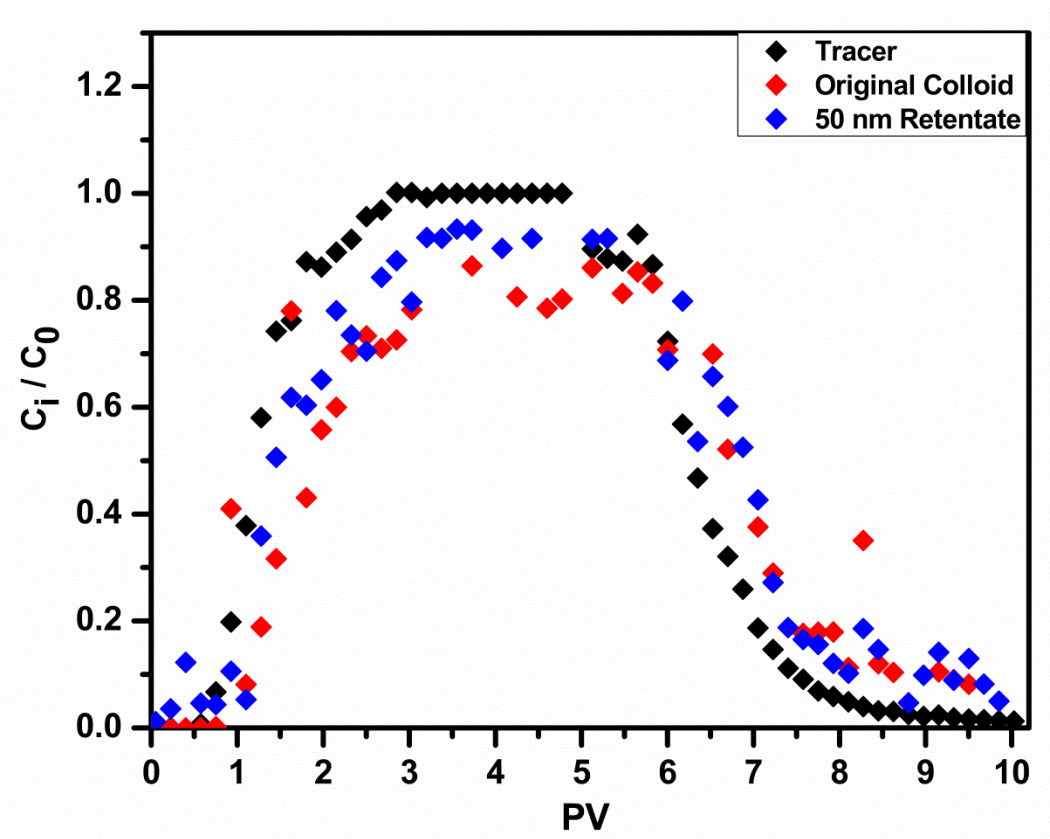

Figure 20: Non-dimensional breakthrough curve of Creighton AgNPs analyzed by FAAS and of Cl^- tracer analyzed by Ion Chromatography measurements. This plot was constructed in *OriginPro 8.5* software at: a depth of 5 cm, influent concentrations of AgNPs of 15.3 mg L^{-1} and KCl of 133 mg L^{-1}, flow rate of 1.0 mL min^{-1}, and fixed pH of 7.8.

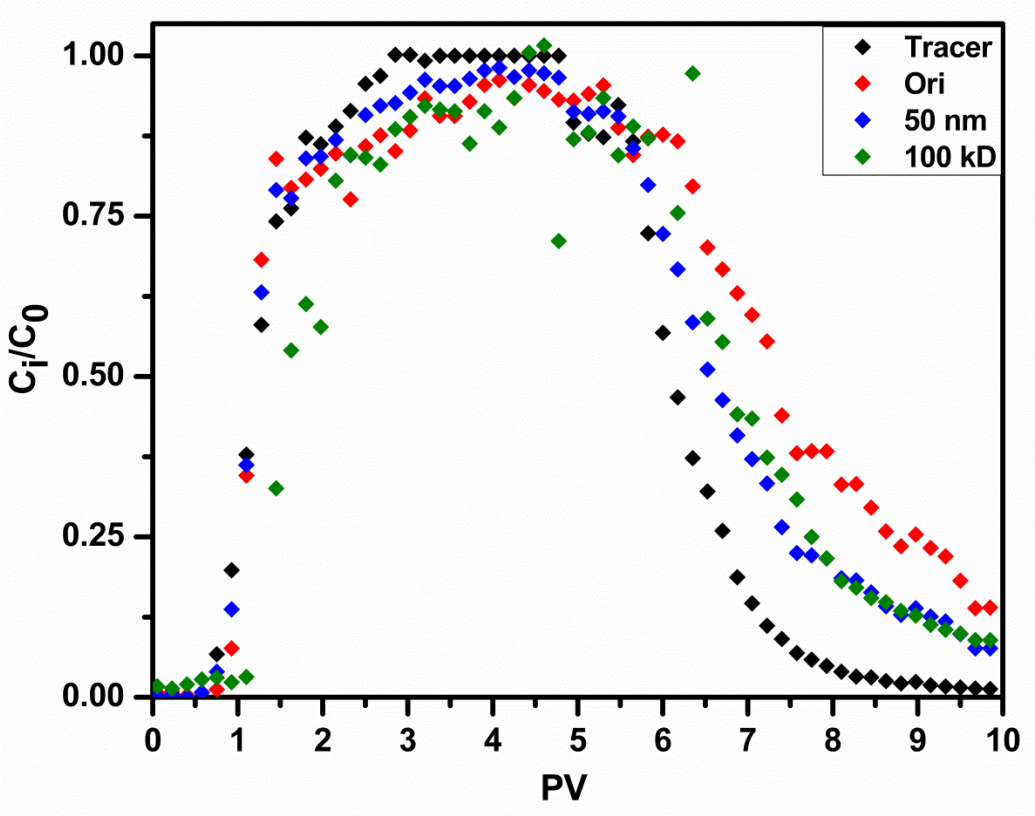

Figure 21: Non-dimensional breakthrough curve of Creighton AgNPs analyzed by UV-Vis absorption spectrophotometry and of the Cl^- tracer analyzed by Ion Chromatography measurements. This plot was constructed in *OriginPro 8.5* software at: depth of 5 cm, influent concentrations of AgNPs of 15.3 mg L^{-1} and KCl of 133 mg L^{-1}, flow rate of 1.0 mL min^{-1}, and fixed pH of 7.8.

Table 4: Acid extraction of AgNPs from the porous media at 5% nitric acid in 45 g of silica.

	Mass Capture	**mg Ag / g Silica**
Original Colloid	25 %	0.001556 ± 0.0002340
50 nm Retentate	30 %	0.002103 ± 0.001315

At 1.0 mL min^{-1}, the breakthrough of AgNPs was delayed compared to the tracer, and the mass capture of AgNPs was about 23% (Table 3). Similar results were observed for the 1.1 mL min^{-1} flow rate as compared to the first case (data not shown). At 2.0 mL min^{-1}, there was less mass capture of AgNPs (9.2%), less tailing (faster desorption), and facilitated transport (AgNPs arrived in the effluent prior to the conservative chloride tracer) (Figure 19 and Table 3). The use of Cl^- ions as tracer was expected to have a minimal effect on the stability of AgNPs during the transport due to the possible formation of silver chloride salt [67]. Facilitated transport was observed for effective flow rate (2 mL min^{-1}) and the negatively charged AgNP Creighton colloid. This is in good agreement with the El Badawy *et al.*'s [68] and Lin *et al*'s [70] studies that reported a **facilitated transport of electrostatically-stabilized AgNPs through unmodified glass beads** probably due to the low affinity of AgNPs to the glass beads [68]. At slower flow rates, the detachment of the AgNPs was slower than their attachment to the highly charged sand media, indicating a higher possibility of equilibrium at the smaller flow rates (Figure 19). AgNPs exhibited **early breakthrough** and a **slight retardation (including tailing during desorption)** with respect to the tracer at comparable flow rates.

AgNP capture within the media was affected by the flow rate and on the average size and size distribution of the AgNPs. The size distribution similarities in broad diameter range for the 50 cc and the original colloid may explain their behavior, specifically their **attachment/detachment rates** with respect to the media. Discrepancies in the 50 cc retentate observed in the size histogram (Figure 12-13) along with presence of aggregates may explain the unexpected effect observed for the larger AgNP size (50-100 nm). In this case, mobility could have been impacted agglomerate particle size [14].

Flow rate and AgNP size distribution were found to influence the sorption of AgNPs to the media and the pattern of the breakthrough curve in distinct manners. Mass capture (indicated by the mass recovery calculations) was increased at slower flow rates and decreased at faster flow rates in agreement with the classical filtration theory (CFT). The AgNP size seemed to affect the rate of desorption by slowing it down. The plateau of the breakthrough peak when the C nears the value of C_0, is sharper for the tracer while it is more round in the case of AgNPs in general, indicating occurrence of diffusion and dispersion of AgNPs.

With respect to the tracer, AgNPs generally exhibited tailing (Figures 19-21) at the end of the desorption phase, indicating that: a) a portion of the influent AgNP mass was captured within the media, b) a portion of the influent AgNP mass was possibly attached to the media irreversibly, and c) the AgNP rate of attachment/detachment was slow due to advection and is indicated by a desorption that is slower than adsorption. This conforms with the previously observed results, where tailing was attributed to reversible capture of CMC-NZVI within the porous

media and where decrease in the size (curve area) of the breakthrough curve was observed alongside with a decline in the C/C_0 [67]. This is among several studies that reported straining as one of the main mechanisms that dominate the capture of NPs within the media. Tufenkji and Raychoudhury *et al.* also attributed the **tailing** effect in the BTC to the detachment of the deposited CMC-NZVI particles from the sand media [67], which is another factor indicating **reversible capture**. The factors observed in this study, in relevance to the mentioned previous study, point to the occurrence of reversible and irreversible capture of AgNPs within the media, as opposed to the classical filtration and coagulation models, which do not account for reversible attachment [62].

According to our results, Creighton colloidal AgNP sorption to the media is found to yield **a non-equilibrium breakthrough and a rate-limited mass transfer,** as indicated by the presence of **tailing**. Furthermore, smaller AgNPs escaped more easily through the saturated pores of the beads. That is due to the impact of various **filtration mechanisms** (straining, sedimentation, interception, and inertial impaction [new ref 61, new ref 62]) on the AgNPs. Larger particles or aggregates are relatively more likely to be captured and removed from the flow by the media [62]. CFT also describes the possibility of particles, driven by "velocity gradients" spatially close to the media-liquid interface, to be attached to the media surface by inertial impaction [61, 62]. Furthermore, attached NPs may amplify the straining process throughout the transport by enhancing the capacity of the collector beads [62]. Possible events that may explain the capture at the low flow rate include the **straining** of larger NPs within an angle formed by adjacent glass beads or the collision of the beads with the

AgNPs [62]. Some discrepancy may be caused by AgNPs traveling close to the media surface as they are likely to experience sedimentation and interception through the pores.

Despite the unpredictability of a contaminant's pathway in subsurface water, it is certain that a colloid's properties will affect its mobility and subsequent accumulation. One limitation of this breakthrough study is that it was not possible to obtain qualitative data on AgNP and silica bead properties in the effluent, such as Raman spectroscopy or Zeta potential for the beads. In regard to the mass capture, it was not possible to determine if degradation [54] or ionic interactions have occurred. AgNP transformation was attributed to factors such as aggregation of AgNPs.

Slightly modified flow rates and/or AgNP sizes influenced AgNP transport according to filtration mechanisms. Physical forces at play mainly relied on advection, dispersion, and chemical forces mainly relied on **electrostatic interactions** between the highly charged porous silica media and the negative AgNP surface.

SPECIFIC AIM 3

3.4. ICP-OES EDUCATIONAL LABORATORY

The novel laboratory module, which targeted the quantification of nanosilver in colloids, was successfully completed by all students in the *Instrumental Analysis* course. Laboratory experiment conditions were well controlled; setup of the lab utilities was prepared beforehand and space was well organized. Recitation material (in form

of Power Point presentations) together with a detailed standard operating procedure (SOP) for the manipulation of the ICP-OES instrument and the preparation of the samples and standards was provided to the students. This allowed them a finer understanding of the presented theoretical aspects and helped them complete the experiment safely and in a time-efficient manner. Students were also provided with recitation slides to review before they were administered a pre-lab quiz related to the working principle of ICP-OES. ICP-OES allowed the control of possible interferences by effectively aerosolizing and ionizing the sample molecules, eliminating the need for ionic suppressors, and allowing two different emission spectral lines in the analysis of Ag. The instrument detection limit for Ag at 328.068 nm was reported to range between 0.5 ppb [102b] and 4.7 ppb [102a] in the axial mode, which agrees well with the value estimated in this study through the standard deviation of the lowest standard.

Equations 1, 4 and 11 illustrate the formulas used by the students for the estimation of the nanosilver concentration in the Creighton colloids. Equation 7 was utilized in conjunction with the external calibration method, while Equation 8 was additionally applied for the standard addition method.

$$\mathbf{C_x = \frac{(V_s)_0\, C_s}{V_x} \times DF} \qquad \textbf{Equation 11}$$

In Equation 11, C_x represents the final concentration of silver in the digested (unspiked) sample of interest, $(V_s)_0$ is the *x*-intercept calculated using Equation 7 at an instrument response of zero, C_s is the concentration of the silver standard used to spike the digested sample aliquots, V_x the volume of the sample aliquots that were spiked, and *DF* is the dilution factor applied for the post-digestion dilution. The *x*-intercept, a negative value delimited by the *y*-axis area from zero instrument response to the first standard addition

(*i.e.*, unspiked AgNP sample), is the volume of standard that corresponds to the amount of analyte in the unspiked sample aliquot.

External calibration and standard addition curves (Figures 20 and 21, respectively) were obtained in the *Instrumental Analysis* laboratory and were utilized in conjunction with Equations 3, 4, and 11 to interpolate the total amounts of silver within the colloidal samples. The external calibration used a direct correlation between concentration and instrument response, allowing direct interpolation by analysis of the linear regression in form of Equation 7. The standard addition utilized both Equations 7 and 8 stepwise as described, allowing to account for matrix effects of the spiked samples in the instrument response.

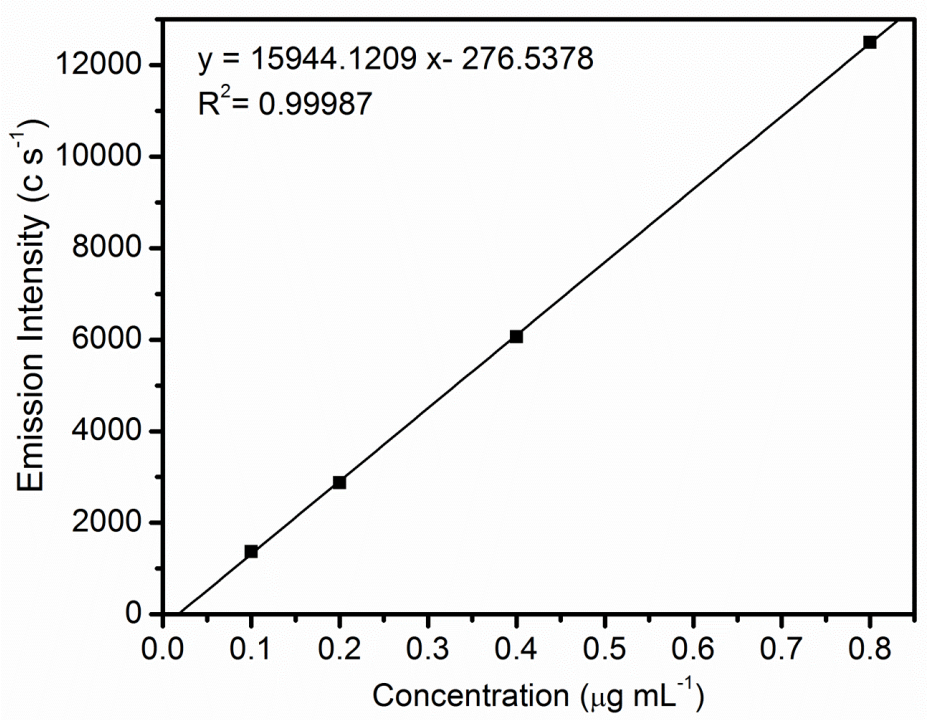

Figure 22: External 4-point calibration curve showing the instrument response as a function of the known standard concentration in the range of 0.1–1.0 μg mL^{-1}.

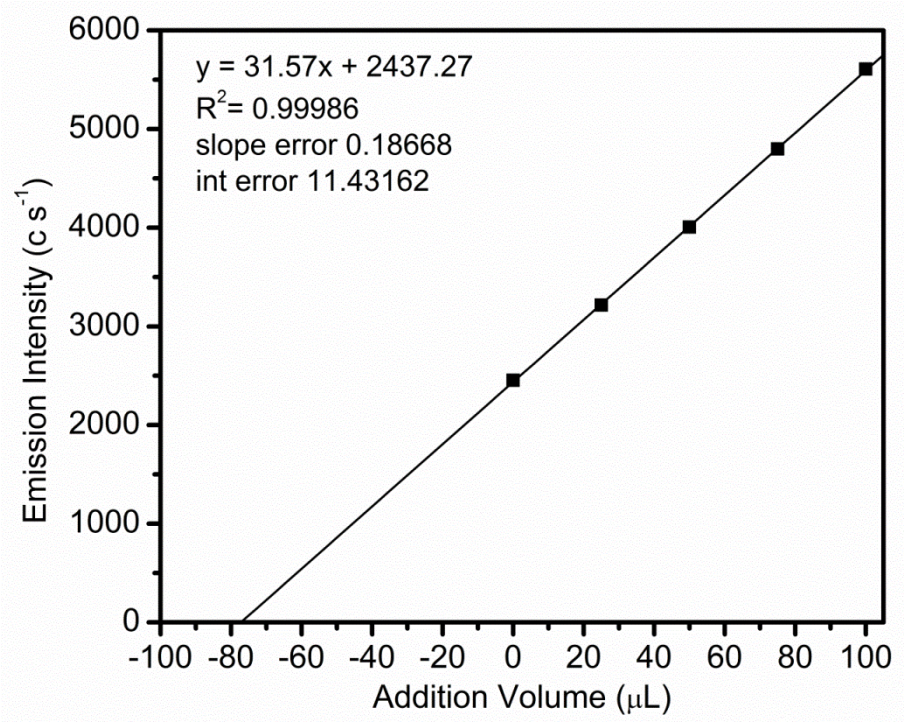

Figure 23: Standard-addition 4-point calibration curve illustrating the instrument response as a function of the volume of the 10 ppm Ag^+ standard added to each standard addition solution.

Theoretically, the standard $AgNO_3$ solution used in the dropwise addition for AgNP synthesis contained 170 ± 5.0 µg mL^{-1} of Ag^+. The Creighton colloidal samples examined by the students were found to contain an average of 15.16 ± 1.58 and 15.20 ± 0.47 µg mL^{-1} by the external calibration and standard addition methods, respectively (Table 5). It should be noted that ICP-OES determines the total Ag amount within the Creighton colloid, which includes any oxidized and free or bound ionic silver. The actual yield obtained using both methods is close to the theoretical yield, which demonstrates the accuracy of the ICP-OES method and the successful synthesis of Creighton AgNPs. The percent difference with

respect to the expected theoretical yield of nanosilver was found to be 1.68% and 1.41% for the external calibration and standard addition methods, respectively. The overall percent difference between the Ag content of the original colloid obtained using the two methods was found to be 0.27%. Thus, the standard addition and the external calibration methods were found to produce equally reliable results for the total silver. The high precision and accuracy of the standard addition method may be attributed to the elimination of matrix interferences, related to aerosol formation and liquid viscosity. ICP-OES yielded relatively higher sensitivity and lower detection limits of Ag with respect to FAAS.

Table 5: Summary of the experimental concentrations of nanosilver obtained by the two lab section groups (a and b) in the *Instrumental Analysis* class calibration methods.

Method	Replicate values	Nanosilver content (µg mL^{-1})	Class average ± S.D. (µg $mL^{-1)}$	Theoretical yield ± S.D. (µg mL^{-1})
Standard Addition	Group a	16.59	15.20 ± 1.95	15.42 ± 0.45
	Group b	13.82		
External Calibration	Group a	15.73	15.16 ± 0.80	
	Group b	14.60		

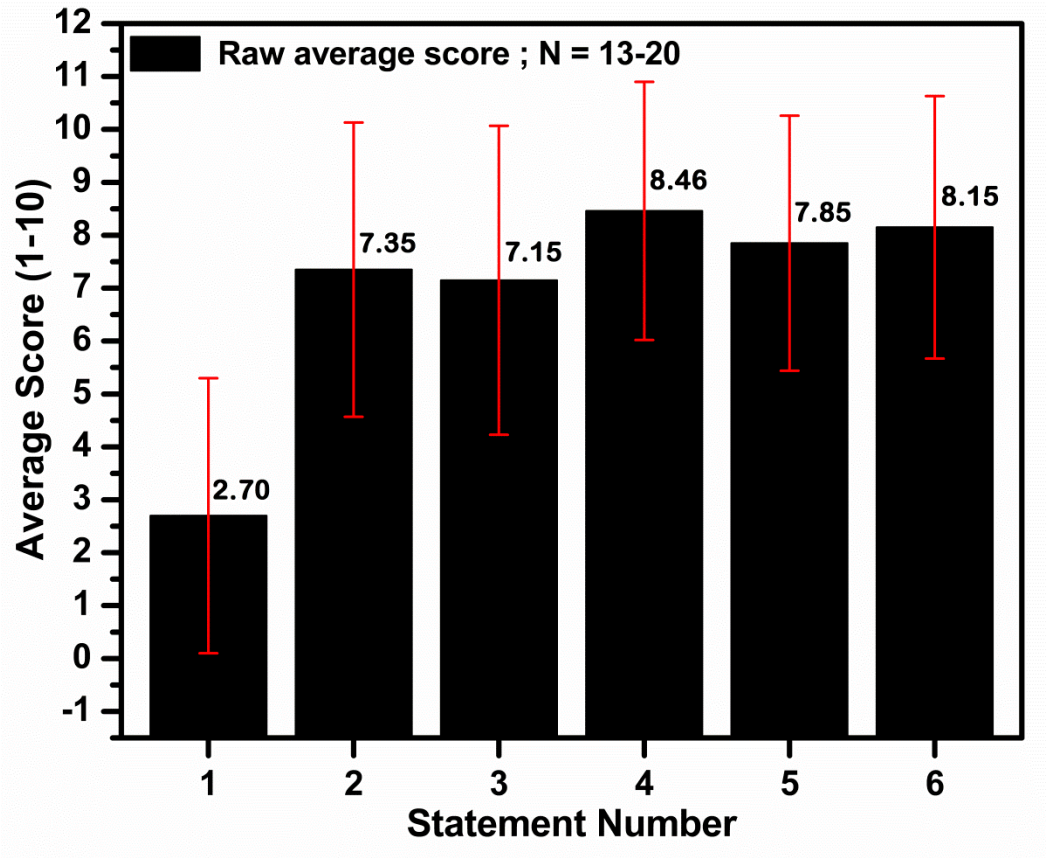

Figure 24: Evaluations of the laboratory experiment, which were administered to the CHM 4350L students (*N* = 13–20), who anonymously assigned scores from "1" to "10", 1 corresponding to a strong disagreement and 10 corresponding to a strong agreement. Evaluations were presented by the graduate teaching assistants in the form of a pre-laboratory questionnaire (*N* = 20), including statements 1-3, and a post-laboratory questionnaire (*N* = 13), including statements 4-6, as follows: 1) "I have no interest in this Instrumental Analysis Laboratory course." ; 2) "I am very interested in the ICP-OES technique."; 3) "I am excited to learn about how the ICP-OES approach may be implemented for the characterization of nanomaterials." ; 4) "My overall experience in this ICP-OES laboratory experiment on nanomaterials was very positive."; 5) "I am very

interested in the ICP-OES technique."; and 6) "I learned a lot in this laboratory experiment."

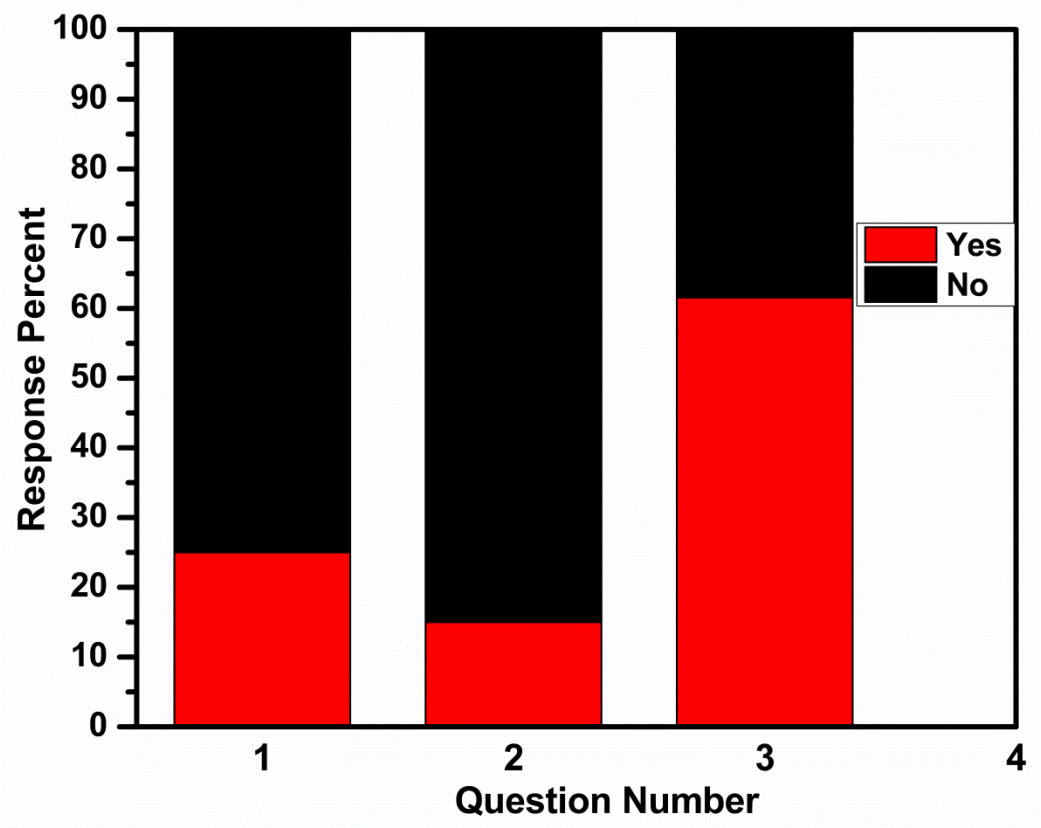

Figure 25: Evaluations of the experiment administered to the CHM 4350L students (N = 13–20), who anonymously answered "Yes" or "No" to the questions presented by the graduate teaching assistants in the form of a pre-laboratory questionnaire (N = 20, questions 1-2) and a post-laboratory questionnaire (N = 13, question 3), as follows: 1) "Have you ever operated an ICP-OES instrument or quantified trace metal samples using other methods prior to this lab experiment?"; 2) "Do you have any experience in the nanotechnology / nanoscience area?"; and 3) "I would like to enroll into a nanotechnology laboratory course that would expand my knowledge in the nanoscience/nanotechnology area." The raw scores were converted into percentages.

Students in the *Instrumental Analysis* course, CHM 435L, were requested to anonymously evaluate the novel ICP-OES laboratory module dedicated to the estimation of the nanosilver amounts in colloids. Figure 24 summarizes the average ratings of the educational aspects that the students volunteered to score. A 6.80% increase in interest was observed throughout the experiment, namely from 7.35 to 7.85, (Questions 2 and 5 respectively, Figure 24). A curve for acquisition of learning and experience was observed throughout the experiment (7.15 to 8.46 and 8.15 (Questions 2, 4, and 6 respectively, Figure 24), corresponding to a 15.10 and 10.88% improvement, respectively. About 25% of students indicated prior knowledge in operation of the ICP-OES instrument and metal quantification, while 15% acknowledged prior experience in the nanotechnology field (Questions 1 and 2, Figure 25). Upon completion of the experiment, 61.54% of the students expressed willingness to enroll in a nanotechnology course (Question 3, Figure 25), which indicates a 50% improvement between the pre- and post- laboratory general response. The drop in the number of participating students, N, (Figures 24, 25) could not be related to the laboratory experiment because it is associated with the students' overall performance in the instrumental analysis lecture and laboratory portions of the course. Were the number of participating students to remain constant throughout the experiment; the scores may have been relatively improved. The notable improvements in learning, experience, and willingness to follow up reflect the benefit students gained during the experiment regardless of their initial knowledge or interest. Positive progress curves resulted due to the increase in the post-lab scores compared to the pre-lab scores. Thus, the novel laboratory module was received well by the students and increased their enthusiasm for nanoscience education. Additional questions were included in the pre-laboratory and post-

laboratory questionnaires, such as “What aspect(s) of this ICP-OES laboratory experiment did you enjoy the most?”; “What aspect(s) should be improved by GTAs and course instructor? Briefly explain why.” and “What aspects were most challenging in this laboratory experiment?” These questions provided feedback for future development of the laboratory module and its instruction.

The students manifested high expectations before and after the experiment completion and expressed interest through asking questions during recitation and a good laboratory attitude. As a result, the participating students were equipped with new laboratory skills related to the sample and standard preparation, the operation of state-of-the-art ICP-OES instrumentation, and the data analysis in Excel and Origin 8 software. Adequate material helped the students succeed at the procedure and justify the outcome with theoretical reasoning, such that they were able to form a comprehensive appreciation of nanomaterials, their properties, uses, and characterization. Concentration is one of the most common standards in nanomaterial characterization because it is needed in both industrial and safety assessment fields. Concentration affects the aggregation state and thus the chemical and physical behavior and shelf life of the NPs [83].

Students gained a rich knowledge of the working principle of the ICP-OES instrument and the advantages and disadvantages of the standard addition and the external calibration methods. As the range of industrial and research applications of AgNPs continue to expand, this new laboratory learning experience will assist science instructors in preparing their students for technologically demanding careers.

4. CONCLUSION

This study allowed the synthesis, size-selection of well characterized Creighton colloidal AgNPs for investigating mobility through the subsurface and ground water. The transport experiment was implemented as an educational module that equipped undergraduate students with knowledge and skills on emerging nanotechnology.

Specific Aim 1 was fulfilled by validating the physicochemical properties of spherical AgNPs (1-100 nm in diameter). The Creighton colloidal AgNPs were shown to have excellent stability and minimal aggregation. The Creighton colloid was size selected via tangential flow filtration to yield two concentrated colloid samples, the "50 cc" and the "100 cc" with AgNP diameters smaller than 20 nm and larger than 50 nm, respectively.

Specific Aim 2 allowed the application of these AgNPs in transport experiments with a setup that modulates the flow of solutes in the subsurface water (saturated porous media). The sorption process depended on the size of the AgNPs, the flow rate, surface charge interactions with the media, and known mechanisms of classical filtration. Lack of symmetry (tailing) and retardation indicated a reversible capture mechanism of AgNPs within the media. Irreversible capture was observed for AgNPs with respect to the tracer upon examining the mass capture (decrease in the area under the breakthrough curve and the C/C_0 ratio remaining below maximum (1). Non-equilibrium sorption at the slower flow rate (1 mL min^{-1}) indicated that attachment/detachment of AgNPs to the silica beads is rate-limited. The transport of the Creighton colloid through the 5 cm-deep media bed was slightly retarded with respect to that of the tracer. Zeta potential measurements showed that the AgNP colloid in general would be resilient to environmental changes. They also aided

in explaining the AgNP facilitated transport of the negatively charged AgNPs through the polar media. When the like charges at the surfaces of the media and the AgNPs undergo electrostatic repulsion, AgNP mobility would increase, enabling a larger mass recovery. On the other hand, mass capture was attributed to irreversible attachment of AgNPs to the media by processes such as particle-media collisions and straining.

Specific Aim 3 allowed for quantification of the AgNP colloids by ICP-OES and the development of an educational module that served to apply nanotechnology skills in the Instrumental Analysis lab taught at WSU. The laboratory experiment allowed students to develop analytical skills by quantifying silver using two calibration ICP-OES methods. Employing the standard addition and the external calibration methods ensured that there would be no matrix effects in the AgNP digested colloids. The students provided excellent feedback on the experience they gained through this educational module. Implementing educational modules, such as this one, will serve to train science students in areas of nanotechnology.

In the future, transport of the widely used, original and size-selected AgNP colloids should be examined in heterogeneous media to better understand breakthrough mechanisms relative to the NP properties (charge, size distribution, concentration, ionic strength, *etc.*). Future work must aim at investigating the possible release of Ag^{+} during the transport as well as the surface interactions of the colloid with the media. Understanding the mobility of ubiquitous colloidal nanoparticles in the subsurface water helps ensure a healthy environment and a clean water supply for generations to come.

5. REFERENCES

1a. United States Environmental Protection Agency. Nanotechnology White Paper. *Office of the Science Advisor/ Science Policy Council* 100/B-07/001 Feb 2007. <www.epa.gov/osa>.

1b. U.S. Environmental Protection Agency. "Nanomaterial Case Study: Nanoscale Silver in Disinfectant Spray (External Review Draft)." Washington DC, U.S., EPA/600/R-10/081, **2010**.

2a. NATIONAL NANOTECHNOLOGY INITIATIVE: Leading to the Next Industrial Revolution - A Report by the Interagency Working Group on Nanoscience, Engineering and Technology Committee on Technology. National Science and Technology Council (NSTC). February 2000 Washington, D.C.

2b. NATIONAL NANOTECHNOLOGY INITIATIVE: Supplement to the President's 2018 Budget - Subcommittee on Nanoscale Science, Engineering, and Technology Committee on Technology National Science and Technology Council (NSTC). November 2017 Washington D.C. <https://www.nano.gov/sites/default/files/NNI-FY18-Budget-Supplement.pdf>.

3. Sargent, John F., Jr. The National Nanotechnology Initiative: Overview, Reauthorization, and Appropriations Issues. *Congressional Research Service* 7-5700, RL34401. May 22, 2012. <www.crs.gov>. Accessed June 2013.

4. European Commission 2010; Commission Recommendation on the definition of the term "nanomaterial; Article 2. <http://ec.europa.eu/environment/consultations/pdf/recommendation_nano.pdf>. 12 Feb 2012.

5a. Project on Emerging Nanotechnologies; Consumer Products; Inventories; Analysis. <http://www.nanotechproject.org/inventories/consumer/analysis_draft/>. March 2013. <http://www.nanotechproject.org/cpi/about/analysis/>.

5b. Vance, M. E.; Kuiken, T.; Vejerano, E. P.; McGinnis, S. P.; Hochella, M. F., Jr.; Rejeski, D.; Hull, M. S., *Beilstein J. Nanotechnol.*, **2015**, *6*, 1769-1780.

6. Kim J. S.; Kuk, E.; Yu, K. N.; Kim, J. H.; Park, S. J.; Lee, H. J.; Kim, S. H.; Park, Y. K.; Park, Y. H.; Hwang, C. Y.; Kim, Y. K.; Lee Y. S.; Jeong, D. H.; Cho,

M. H., .*Nanomedicine: Nanotechnology, Biology, and Medicine* **2007**, *3* (1), 95–101.

7. Trefry, John C. Ph.D . Dissertation. The development of silver nanoparticles as antiviral agents. Wright State University, May 13, 2011.

8. Rai , M.; Yadav, A.; Gade, A., *Biotechnology Advances* **2009**, *27* (1), 76–83.

9. Alexander, J. W., *Surgical Infections* **2009**, *10* (3), 289–292.

10. Chen, X.; Schluesener, H. J., *Toxicology Letters* **2008**, *176*: 1–12.

11. Klippstein, R.; Fernandez-Montesinos, R.; Castillo, P. M.; Zaderenko, A. P., *Silver Nanoparticles* (Perez, D. P., Ed.), (2010)., Ch. 16, InTech. ISBN 978-953-307-028-5. <http://www.intechopen.com/books/silver-nanoparticles>.

12. Politano, A. D.; Campbell, K. T.; Rosenberger, L. H.; Sawyer, R. G., *Surgical Infections* **2013,** *14* (1), 8–20. <http://online.liebertpub.com/doi/full/10.1089/sur.2011.097>.

13. El-Sayed, M. A.; Eustis, S., *Chemical Society Reviews* **2006**, *35*, 209– 217.

14. Oberdorster. "Nanomaterials in Reach: Project report. 15 August **2011**." UCM214304.pdf (application/pdf object).

15. Nowack, B.; Krug, H. F.; Height, M., *Environmental Science and Technology* **2011**, *45* (4), 1177–1183.

16. Freestone, I.; Meeks, N.; Sax, M.; Higgit, C., *Gold Bulletin* **2007**, *4* (40), 270–277.

17. Gong, Ping; Li, Huimin; He, Xiaoxiao; Wang, Kemin; Hu, Jianbing; Tan, Weihong; Zhang, Shouchun; and Yang, Xiaohai. Preparation and antibacterial activity of Fe3O4@Ag nanoparticles. *Nanotechnology* **2007**, *18* (28), 285–604.

18. Soltani, M., Ghodratnema, M.; Ahari, H.; Ebrahimzadeh Mousavi, H. A.; Atee, M., Dastmalchi, F.; Rahmanya, J., *International Journal of Veterinary Research* **2009**, *3* (2), 137–142.

19. Oyanedel-Craver, V. A.; Smith, J. A., *Environmental Science and Technology* **2008**, *42* (3), 927–933.

20. Pradreep, T.; Anshup, *Thin solid film*s **2009**, *517*, 6441−6478.

21. Mirkin, C. A.; Cao, Y. C.; Jin, R., *Science* **2002**, *297*, 1536–1540.

22. Stoeva, S. I.; Lee, J.-S.; Smith, J. E.; Rosen, S. T.; Mirkin, C. A., *Journal of the American Chemical Society* **2006**, *128* (26), 8378–8379.

23. Zheng, W.; He, L., *Analytical and Bioanalytical Chemistry* **2010**, *397*, 2261–2270.

24. Lin, J.; Chen, R.; Feng, S.; Pan, J.; Li, Y.; Chen, G.; Cheng, M.; Huang, Z.; Yu, Y.; and Zeng, H., *Nanomedicine: Nanotechnology, Biology, and Medicine* **2011**, *7*: 655–663.

25. Ruizhi, X.; Ma, J.; Sun, X.; Chen, Z.; Jiang, X.; Guo, Z.; Huang, L.; Li, Y.; Wang, M.; Wang, C.; Liu, J.; Fan, X.; Gu, J.; Chen, X.; Zhang, Y.; Gu, N., *Cell Research* **2009**, *19* (8), 1031−1034.

26. Govender, R.; Phulukdaree, A.; Gengan, R. M.; Anand, K.; Chuturgoon, A. A. *Journal of Nanobiotechnology* **2013**, *11* (5). doi:10.1186/1477-3155-11-5.

27. Linic, S.; Christopher, P.; Ingram, D. B., *Nature Materials* **2011**, *10* (12), 911–921.

28. Oldenburg, S. J. "Silver Nanoparticles: Properties and Applications." *Sigma-Aldrich Materials Science*. Copyright 2013. Web. 21 March **2013**. <http://www.sigmaaldrich.com/materials-science/nanomaterials/silver-nanoparticles.html>. Accessed March 2013.

29. Singh, S. N.; Rudra, R.; Tripathi, D. (Eds)., *Environmental Bioremediation Technologies*, New York, Springer-Verlag Berlin Heidelberg, **2007**, p. 218–220.

30. Luoma, S.N. "Silver Nanotechnologies and the Environment: Old Problems or New Challenges?" Woodrow Wilson International Center for Scholars Project on Emerging Nanotechnologies and The Pew Charitable Trusts, September **2008**.

31. Hu, Z. “Impact of Silver Nanoparticles on Wastewater Treatment; Final Report.” *Water Environment Research Foundation (WERF)* **2010**.

32. Free Drinking Water. Water Quality; The Truth About Our Environment and Water. <http://www.freedrinkingwater.com/water-purification-need.htm>. Accessed December 2012.

33. Seiler, H. G.; Sigel, A.; and Sigel, H. *Handbook on metals in clinical and analytical chemistry*, 18th Ed., New York, M. Dekker. (Harvard), 1994.

34. Schulte, P. A.; Murashov, V.; Zumwalde, R.; Kuempel, E. D.; Geraci, C. L., *Journal of Nanoparticle Research* **2010**, *12* (6), 1971–1987.

35. Ford, L. *Water Environment Research* **2001**, *73* (2), 248–253.

36a. Agency for Toxic Substances and Disease Registry; Toxicological Profile for Silver, Department of Health and Human Services, Public Health Service. Atlanta, GA, December **1990**.

36b. World Health Organization (WHO) Report on regulations and standards for drinking-water quality. November **2013**, *Draft 12*.

37. Drake, P. L.; Hazelwood, K. J., *Annals of Occupational Hygiene* **2005**, *49* (7), 575–585.

38. Langmuir, D.; Chrostowski, P.; Vigneault, B.; Chaney, R., *Issue Paper on the Environmental Chemistry of Metals.* U.S. Environmental Protection Agency 1995 Draft, and August 2004 publication.

39. Benn, T. M.; Westerhoff, P., *Environ. Sci. Technol*. **2008**, *42* (11), 4133–4139.

40. Hund-Rinke, K.; Marscheider-Weidemann, F.; Kemper M. “Beurteilung der Gesamtumweltexposition von Silberionen aus Biozid-Produkten” [Assessment of the overall environmental exposure of silver ions from biocidal products]. *Umweltbundesamtes*, **2008**, Texte 43/08.

41. Mueller, N. C.; Nowack, B. *Environmental Science and Technology* **2008**, *42* (12), 4447–4453.

42. Tolaymat, T. M.; El Badawy, A. M.; Genaidy, A.; Scheckel, K. G.; Luxton, T. P.; Suidan, M., *Science of the Total Environment* **2010**, *408* (5), 999–1006.

43. El-Ansary, A.; Al-Daihan, S., *Journal of Toxicology* **2009**, *754810*, 1–9.

44. Geisler-Lee, J.; Wang, Q.; Yao, Y.; Zhang, W.; Geisler, M.; Li, K.; Huang, Y.; Chen, Y.; Kolmakov, A.; and Ma, X., *Nanotoxicology* **2012**, *7*(3), 323–337.

45. El Badawy, A. "Assessment of the fate and transport of silver nanoparticles in porous media. Dissertation" **2011**.

46. Sharma, H. S.; Ali, S. F.; Tian, Z. R.; Hussain, S. M.; Schlager, J. J.; Sjöquist, P. O.; Sharma, A.; Muresanu, D. F., *Journal of Nanoscience and Nanotechnology* **2009**, *9* (8), 5073−5090.

47. Kumari, M.; Mukherjee A.; Chandrasekaran, N., *Science of the Total Environment* **2009**, *407* (19), 5243-5246.

48. Pal, S.; Tak, Y. K.; Song, J. M., *Applied and Environmental Microbiology* **2007**, *27* (6), 1712–1720.

49. Liu W.; Wu, Y.; Wang, C.; Li, H. C.; Wang, T.; Liao, C.; Cui, L.; Zhou, Q. F.; Yan, B.; Jiag, G. B., *Nanotoxicology* **2010**, *4* (3), 319–330.

50. Senjen, Rye; Friends of the Earth Australia and Ian Illuminato; Friends of the Earth United States. "Extreme Germ Killers Present a Growing Threat to Public Health." *NANO & BIOCIDAL SILVER*, June 2009.

51. Lee Y. J.; Kim, J.; Oh, J.; Bae, S.; Lee, S.; Hong, I. S.; Kim, S. H.. Ion-release kinetics and ecotoxicity effects of silver nanoparticles. *Environ Toxicol Chem*. **2012**, *31* (1), 155–159.

Jomova, K.; Valko, M., *Toxicology* **2011**, *283* (2–3), 65–87.

53a. Sotiriou, G. A.; Pratsinis, S. E., *Current Opinion in Chemical Engineering* **2011**, *1*, 3–10.

53b. Liu, J.; Sonshine, D.A.; Shervani, S.; Hurt, R. H., *ACS Nano* **2010**, *4* (11), 6903–6913.

53c. Liu, J.; Hurt, R. H., *Environ. Sci. Technol.* **2010**, *44* (6), 2169–2175.

54. Ward, C. H.; Cherry, J. A.; Scalf, M. R. (1997). *Subsurface Restoration*. Ann Harbor Press, Inc. MI.

55. Southeastern Virginia planning district commission. Groundwater protection handbook for Southeastern Virginia. *U.S. Government Printing Office*, January 1990. http://www.gpo.gov/. Source: Virginia State Water Control Board, 1989.

56. Water Treatment Solutions Lenntech. Groundwater. http://www.lenntech.com/groundwater/properties.htm. 2013.

57. Baalousha, M.; Manciulea, A.; Cumberland, S.; Kendall, K.; Lead, J.R., *Environmental Toxicology and Chemistry* **2008**, *27* (9), 1875−1882.

58. Christian, P.; Von Der Kammer; F.; Baalousha; M.; Hofmann; T., *Ecotoxicology* **2008**, *17* (5), 326−343.

59. Hu, J.-D.; Zevi, Y.; Kou, X-M.; Xiao, J.; Wang, X-J.; Jin, Y., *Science of the Total Environment* **2010**, *408*, 3477−3489.

60. Delay, M.; Dolt T.; Woellhaf, A.; Sembritzki, R.; Frimmel, F. H. Interactions and stability of silver nanoparticles in the aqueous phase: Influence of natural organic matter (NOM) and ionic strength. *Journal of Chromatography A* **2011**, *1218* (27), 4206–4212.

61a. Jegatheessan, V.; Vigneswaran, S., (Keir, G., Ed.). "Deep Bed Filtration: Modeling Theory and Practice. Water and Wastewater Technologies." (2009) *Encyclopedia of Life Support Systems*, Oxford, United Kingdom. <http://www.eolss.net/Sample-Chapters/C07/E6-144-08.pdf>.

61b. Ahmad, S.; and Simonovic, S. P. Comparison of One-Dimensional and Two-Dimensional Hydrodynamic Modeling Approaches For Red River Basin. Final Report to) *International Joint Commission*, December **1999**.

62. Yao, K.-M.; Habibian, M. T.; and O'Melia, C. R., Environmental Science and Technology, **1971**, *5* (11), 1105-1112.

63. Tufenkji, N.; Elimelech, M., *Environmental Science and Technology*, **2004b**, *38* (2), 529–536.

64. Virtual Library of Sustainable Development and Environmental Health "Transport and fate of contaminants in the subsurface". In: Handbook ground water; volume II, methodology Environmental Protection Agency. <http://www.bvsde.opsoms.org/muwww/fulltext/repind46/transport/transport.html. 5/16/2002. Accessed September 2013.

65. Tufenkji, N.; Elimelech, M., *Langmuir* **2005**, *21* (3), 841-852.

66. Wang, Y.; Kim, J-H.; Baek, J-B.; Miller, G. W.; Pennell, K. D. "Transport behavior of functionalized multi-wall carbon nanotubes in Water-saturated quartz sand as a function of tube Length." *Water Research* **2012**. (In press/accepted manuscript).

67. Raychoudhury, T.; Tufenkji, N.; Ghoshal, S., *Water Research* **2014**, *50*, 80–89.

68. El Badawy, A.M.; Hassan, A.A.; Scheckel, K.G.; Suidan, M.T.; and Tolaymat, T.M., *Environmental Science and Technology* **2013**, *47*, 4039–4045.

69a. El Badawy, A. M.; Luxton, T. P.; Silva, R.; Scheckel, K. G.; Suidan, M. T.; Tolaymat T., *Environmental Science and Technology* **2010**, *44* (4), 1260–1266.

69b. Qin, D.; Riggs, B. "Nanotechnology: Top-Down Approach." *Encyclopedia of Supramolecular Chemistry*. DOI: 10.1081/E-ESMC-120047104, Taylor & Francis, (2012).

70a. Lin, S.; Cheng, Y.; Bobcombe, Y.; Jones, K. L.; Liu, J.; and Wiesner, M. R., *Environmental Science and Technology* **2011**, *45*, 5209–5215.

70b. Suneel, Sri D. "Nanotechnology". Nano Technology (Elective) - F 4823. *Gitam University*. <http://www.gitam.edu/eresource/nano/nanotechnology/nanotechnology%20web%201.htm>. Accessed May 2013.

71. Bittner, M.; Wu, X. C.; Balci, S.; Knez, M.; Kadri, A.; Kern, K., *European Journal of Inorganic Chemistry* **2005**, *2005* (8), 3717–3728. <www.eurjic.org>.

72. Cioffi, N.; and Rai, M. *Nano-antimicrobials: Progress and Prospects, 1st Ed*. Springer-Verlag New York, LLC, **2012**. <http://www.barnesandnoble.com/w/nano-antimicrobials-nicola-cioffi/1110841521?ean=9783642244278>.

73. Sharma, S. K.; Mudhoo, A. (Eds). *Green Chemistry for Environmental Sustainability, 1st Ed*. CRC Press, **2010**. <http://www.barnesandnoble.com/w/green-

chemistry-for-environmental-sustainability-sanjay-kumar-sharma/1101367249?ean=9781439824733&isbn=9781439824740>.

74. Sarkar, Dibyendu; Datta, Rupali; Hannigan, Robyn (Eds). *Concepts and Applications in Environmental Geochemistry* (Developments in Environmental Science 5). Ch. 21, Elsevier Science, 2007. <http://www.barnesandnoble.com/w/concepts-and-applications-in-environmental-geochemistry-dibyendu-sarkar/1100664983?ean=9780080465227&isbn=9780080549736>.

75. Creighton, J. A.; Blatchford, C. G.; Albrecht, M. G., *Journal of the Chemical Society, Faraday Transactions* **1979**, *2* (75), 790.

76. Pavel, I. E.; Alnajjar, K. S.; Monahan, J. L.; Stahler, A.; Hunter, N. E.; Weaver, K. M.; Baker J. D.; Meyerhoefer, A. J.; Dolson, D. A., *Journal of Chemical Education* **2012**, *89*, 286–290.

77. Link, S.; El Sayed, M. A. *Int. Review in Physical Chemistry* **2000**, *19* (3), 409–453.

78. Anastas, P.T.; and Warner, J. C. "Green Chemistry: Theory and Practice", *Oxford University Press*: New York, **1998**, p.30.

79. Millipore. "Protein concentration and diafiltration by tangential flow filtration." *Millipore Corporation* **2003**, TB032. (Millipore technical publications, <http://www.millipore.com/techpublications/tech1/tb032>. Accessed June 2013.

80. Spectrum Laboratories. Chemical compatibility of membranes. <http://www.spectrumlabs.com/dialysis/Compatibility.html>.

81. Schwartz, L.; and Seeley, K. "Introduction to tangential Flow Filtration for Laboratory and Process Development Applications." Pall Corporation. <http://www.pall.com/main/laboratory/literature-library-details.page?id=34212>. Accessed 2013-2018.

82. Anders, C. B.; Baker, J. D.; Stahler, A. C.; Williams, A.; Sisco, J. N.; Trefry, J. C., Wooley, D. P.; Pavel Sizemore, I. E., *Journal of Visualized Experiment* **2012**, *4* (68), 1–9. <http://www.ncbi.nlm.nih.gov/pubmed/23070148>.

83. Trefry, J.C.; Monahan, J. L.; Weaver, K. M.; Meyerhoefer, A. J.; Markopoulos, M. M.; Arnold, Z. S.; Wooley, D. P.; Pavel, I. E., *Journal of the American Chemical Society* **2010**, *132* (32), 10970–10972.

84a. Paluri; S. L. A., Ph.D. Thesis Dissertation. Analytical-based methodologies to examine in vitro nanokinetics of silver nanoparticles. Wright State University, April 2017.

84b. Paluri, S. L. A.; Ryan, J. D.; Lam, N. H.; Nepal, D.; Sizemore Pavel, I. E. "Analytical-Based Methodologies for Examining the In Vitro Absorption, Distribution, Metabolism, and Elimination (ADME) of Silver Nanoparticles." *Small* **2017**, *13*, 16030-93.

85. Skoog, D. A.; Holler, F. J.; and Crouch, S. R. *Principles of instrumental analysis*. Brooks/Cole Pub Co, Belmont, CA, 2007; Vol. 6th Ed.

86. Ershov, B. G.; Gordeev, A. V., *Mendeleev Community* **2001**, *11* (4), 147–148.

87. Lin-Vien, D.; Colthup, N. B.; Fateley, W. G.; Grasselli, J. G. *Handbook of Infrared and Raman Characteristic Frequencies of Organic Molecul*es. Academic Press: San Diego, CA, 1991.

88. Voutoum, B.; Stefanaki, E-C., *Electron Microscopy: The Basics*. Physics of Advanced Materials Winter School 2008.

89. Nanoscale Engineering Science and Technology. "Hitachi H-7600 transmission electron microscope (TEM)." http://nestlaboratory.com/documents/contentdocuments/61.pdf. Revised April 2006. Accessed January 2013.

90a. Brookhaven particle size standards and microspheres. <http://www.brookhaven.co.uk/dynamic-light-scattering.html>. Accessed Aug 2013.

90b. McNaught, A. D. and Wilkinson, A. in "IUPAC. Compendium of Chemical Terminology", 2nd ed. of the "Gold Book" by. Blackwell Scientific Publications, Oxford (1997). Zeta Potential Using Laser Doppler Electrophoresis at <www.malvern.com>.

91a. Pfaff, J. D.; EPA, Method 300.0: Determination of inorganic anions by ion chromatography; Revision 2.1 August **1993**; revision August 2009.

91b. Environmental Sciences Section. “ESS Method 200.5. “Determination of Inorganic Anions in Water by Ion Chromatography.” Inorganic Chemistry Unit, Wisconsin State Lab of Hygiene, October **1992**.

92. Ptak, T.; Piepenbrink, M.; Martac, E., *Journal of Hydrology* **2004**, *294*, 122–163.

93. Andreiadis, E. S., “Breakthrough curves, determination of specific parameters.” *Polytech University of Bucharest*, **2005**.

94. Brusseau, M. L.; Rao, P. S. C. *Journal of Contaminant Hydrology* **1989**, *4* (3), 223–240.

95. Boss, C. B.; Fredeen, K. J. “Concepts, Instrumentation and techniques in Inductively coupled plasma optical emission spectrometry”, (1997), *3.1*.

96. Hou, X.; Jones, B. T. (2000). *Inductively Coupled Plasma/Optical Emission Spectrometry. Encyclopedia of Analytical Chemistry.* Meyers, R. A. (Ed.) Copyright Ó John Wiley & Sons Ltd. pp. 9468–9485.

97. Olesik, J. W. “Elemental Analysis Using ICP-OES and ICP/MS.” *Analytical Chemistry* **1991**, *63*, 12A–21A.

98. Agilent Technologies. Agilent 710 Series ICP-OES. Agilent Technologies Inc. September 2010. 5990-6496EN.

99. Robinson, J. W.; Frame, E. M. S.; and Ii Frame, G. M. (2005). *Undergraduate Instrumental Analysis*. Marcel Dekker: NY, Vol. 6th ed., p 483–505.

100. The Linde Group. Industries; Laboratories; Analysis and Measurement; Inductively Coupled Plasma. <http://www.lindeus.com/en/industries/laboratories/analysis_and_measurement/inductively_coupled_plasma/>. Accessed January 2013.

101. Savas, S. Inductively Coupled Plasma for Highly Efficient and Low Damage Resist Stripping. *Mattson Technology, Inc. Fremont, CA 94538.*

102a. Environmental Protection Agency (2007). Method 6010C; Inductively Coupled Plasma-Atomic Emission Spectrometry. Revision 3.

102b. Hannan, J. “US EPA Method 200.7 using the Thermo Scientific iCAP 7600 ICP-OES Duo” *Thermo Fisher Scientific*, Cambridge, UK. <http://www.acm2.com/prilojenia/Atomno%20emisionni/AN43157_US%20EPA%20200.7.pdf>. Accessed 2013-2018.

103. Vanclay, E. Guidelines for Trouble Shooting and Maintenance of ICP-OES Systems. May 2, **2012**.

104. Dunnivant, F. M.; Ginsbach, J. W. (2009). *Flame Atomic Absorbance and Emission Spectroscopy and Inductively Coupled Spectrometry - Mass Spectrometry*. Whitman College, WA, Ch 3. http://people.whitman.edu/~dunnivfm/FAASICPMS_Ebook/Downloads/index.html .

105. Bader, M. A. A systematic approach to standard addition methods in instrumental analysis. *Jour. Chem. Ed.* **1980**, *57* (10), 573.

106. U. S. Environmental Protection Agency. Method 7760A; Silver (atomic absorption, direct aspiration). Revision 1 July 1992.

107. Martina, I.; Wiesinger, R.; Jembrih-Simburger, D.; and Schreiner, M. Micro-Raman characterization of silver corrosion products: instrumental set up and reference database. *E-PRESERVATION Science* **2012**, *9*, 1–8.

108. American Public Health Association, American Water Works Association, and Water Environment Federation. “Standard Methods for the Examination of Water and Wastewater.” 1999.

109. Baker, J., M.S. Thesis Dissertation. “Near single-molecule SERS–based detection using ultrafiltered, unfunctionalized silver nanoparticles.” Wright State University, June 2012.

110. Brusseau, M. L., *Environmental Science and Technology* **1991**, *25*, 134–142.

111**.** Magdassi, S.; Bassa, A.; Vinetsky, Y.; and Kamyshny, A., *Chemistry of Materials* **2003**, *15* (11), 2208–2217.

112. Alvarez-Puebla, R.A.; Arceo, E.; Goulet, P. J. G.; Garrido, J. J.; Aroca, R. F., *The Journal of Physical Chemistry B* **2005**, *109*, 3787–3792.

113. Flory, J.; Kanel, S. R.; Racz, LA.; Impellitteri, C. A.; Silva, R. G.; Goltz, M. N., *Journal of Nanoparticle Research* **2013**, *15*, 1484.